Vol. 45 — N° 1 03 21 P. 161 – 187

GEOSTANDARDS and GEOANALYTICAL RESEARCH

In Situ Oxygen Isotope Determination in Serpentine Minerals by SIMS: Addressing Matrix Effects and Providing New Insights on Serpentinisation at Hole BA1B (Samail ophiolite, Oman)

Maria Rosa **Scicchitano** (1)*, Michael J. **Spicuzza** (1), Eric T. **Ellison** (2), David **Tuschel** (3), Alexis S. **Templeton** (2) and John W. **Valley** (1)

(1) Department of Geoscience, University of Wisconsin, Madison, WI, USA
(2) Geological Sciences, University of Colorado-Boulder, Boulder, CO, USA
(3) HORIBA Scientific, Piscataway, NJ, USA
* Corresponding author. e-mail: mscicchitano@wisc.edu

The ability to constrain the petrogenesis of multiple serpentine generations recorded at the microscale is crucial for estimating the extent and conditions of modern *versus* fossil serpentinisation in ophiolites. To address matrix bias effects during oxygen isotope analysis by SIMS, we present the first investigation analysing antigorite in the compositional range Mg# = 77.5–99.5 mole %, using a CAMECA IMS-1280 secondary ion mass spectrometer. Spot-to-spot homogeneity is ≤ 0.5‰ (2s) for the new antigorite reference materials. The relative bias between antigorite reference materials with different Mg/Fe ratios is described by a second-order polynomial, and a maximum difference in bias of ~ 1.8‰ was measured for Mg# ~ 78 to 100. We observed a bias up to ~ 1.0‰ between lizardite and antigorite attributed to their different crystal structures. Orientation effects up to ~ 1‰ were observed in chrysotile. The new analytical protocol allowed the identification of oxygen isotope zoning up to ~ 7‰ in serpentine minerals from two serpentinites recovered from an area of active serpentinisation in the Samail ophiolite. Thus, *in situ* analysis is capable of resolving isotopic heterogeneity that may directly reflect changes in the physical and chemical conditions of multiple serpentinisation events in the Samail ophiolite.

Keywords: serpentine, Oman, oxygen isotopes, SIMS, reference materials.

Received 23 Apr 20 – Accepted 24 Aug 20

Serpentinites, derived from ultramafic rocks that have undergone extensive water/rock interaction and hydration, have generated great interest recently because of the crucial role they play in: (i) recycling water and trace elements between the Earth's crust and the upper mantle where the dehydration of altered seafloor serpentinites in subduction zones induces mantle melting at sub-arc depths (e.g., Scambelluri *et al.* 2004, Hattori and Guillot 2007, Deschamps *et al.* 2010, Alt *et al.* 2012, Marchesi *et al.* 2013, Barnes *et al.* 2014); (ii) providing a suitable habitat for the origin and early development of life in the early Earth and potentially other planetary bodies by generating energy and H_2-rich fluids (e.g., Früh-Green *et al.* 2004, Sleep *et al.* 2004, Kelley *et al.* 2005, McCollom and Seewald 2013, Schrenk *et al.* 2013); and (iii) the possible mitigation of global warming due to their ability to securely store carbon dioxide through mineral carbonation reactions (e.g., Andreani *et al.* 2008, Kelemen and Matter 2008, Kelemen *et al.* 2011, Schwarzenbach *et al.* 2013).

Serpentinites are often characterised by complex anastomosing networks of veins with different serpentine generations resulting from multiple stages of rock–fluid interaction that occur at varying temperatures and/or with chemically or isotopically distinct fluids (e.g., Andreani *et al.* 2007, Kahl *et al.* 2015). Consequently, a thorough understanding of the conditions at which serpentinisation occurred and its effects on processes taking place at the interface between the solid earth, the hydrosphere, the atmosphere and the biosphere relies on the ability to constrain each of these hydration events. Physical–chemical properties of rock–fluid interaction processes, such as temperature, fluid source and flux, can be investigated using oxygen isotope ratios, which span a range of ~ 100‰ in the Earth's crust and mantle (e.g., Valley

doi: 10.1111/ggr.12359

et al. 2005). Consequently, $\delta^{18}O$ variations in minerals due to interaction with fluids in isotopic disequilibrium with the bulk rock can be detected as long as volumetrically significant mass transformations occur (Bindeman 2008). The microscale textural relations often observed in serpentinites require the use of *in situ* microanalytical techniques to resolve and properly interpret the evidence for multiple serpentinisation events. *In situ* microanalysis of oxygen isotope ratios in minerals is only possible by secondary ion mass spectrometry (SIMS), which allows isotopic data to be correlated with other geochemical information in petrological context (Valley and Kita 2009).

However as a comparative technique, SIMS requires the use of matrix-matched reference materials (RMs) due to the occurrence of analytical artefacts, called bias, affecting the measured isotopic ratios (Valley and Kita 2009). Previous studies performed with large-radius multi-collector secondary ion mass spectrometers (CAMECA IMS-1270 and 1280, SHRIMP II and SI instruments) showed that matrix effects, the component of bias caused by the chemical and/or structural state of the sample, are variable for most minerals with significant solid solution, such as garnet (Vielzeuf *et al.* 2005, Page *et al.* 2010, Martin *et al.* 2014, Gauthiez-Putallaz *et al.* 2016), olivine (e.g., Valley and Kita 2009, Tenner *et al.* 2015, Isa *et al.* 2017, Scicchitano *et al.* 2018b), plagioclase (Valley and Kita 2009), alkali feldspar (Pollington 2013), ortho- and clinopyroxenes (Valley and Kita 2009, Kita *et al.* 2010, Tenner *et al.* 2015), monazite (Rubatto *et al.* 2014), titanite (Bonamici *et al.* 2011), biotite (Siron *et al.* 2017) and carbonates (e.g., Valley and Kita 2009, Rollion-Bard and Marin-Carbonne 2011, Śliwiński *et al.* 2017). Without an accurate estimate of matrix effects on bias across mineral solid solutions, SIMS analyses conducted on unknown samples using a single or a limited number of reference materials may not be accurate.

Scicchitano *et al.* (2018a) developed the first set of serpentine reference materials for *in situ* measurement of oxygen isotope ratios by sensitive high-resolution ion microprobe (SHRIMP), one per each of the common polymorphs antigorite (sample Al06-44A, Mg# = 94.6 mole %), lizardite (sample L3431, Mg# = 98.3 mole %) and chrysotile (sample C22908, Mg# = 98.1 mole %). The new analytical protocol confirmed the effectiveness of SIMS techniques in unravelling heterogeneities in oxygen isotope compositions of serpentine at the microscale that would otherwise be concealed by bulk analyses (Rouméjon *et al.* 2018, Scicchitano *et al.* 2018b). Nevertheless, Scicchitano *et al.* (2018a) did not investigate matrix effects across varying Mg/Fe ratios in serpentine given only one reference material per polytype was available. Because serpentine can contain variable amount of iron (e.g., Mg# ~ 78–99 mole %; Evans *et al.* 2009, 2012, Mayhew and Ellison 2020) and of matrix effects that contribute to bias during SIMS analysis related to Mg/Fe variations in some minerals (e.g., olivine, carbonates; e.g., Kita *et al.* 2010, Śliwiński *et al.* 2015, Isa *et al.* 2017, Scicchitano *et al.* 2018b), further analytical developments are required to ensure the accuracy of *in situ* oxygen isotope measurements for the full compositional spectrum of serpentine minerals observed in various natural environments.

We present the first investigation of matrix effects related to variation in the Mg/Fe ratio in serpentine using a CAMECA IMS-1280 secondary ion mass spectrometer at the WiscSIMS Laboratory (University of Wisconsin-Madison, UW-Madison). New antigorite samples, in addition to Al06-44A, were selected for detailed study because chemically and isotopically homogeneous material with variable Mg/Fe content was identified. In contrast, no pure and isotopically homogenous material of the lizardite and chrysotile polymorphs, spanning a comparably large Mg/Fe range, was identified as suitable reference materials for SIMS analysis. We evaluated relative bias between antigorite and the other two serpentine polymorphs commonly found in nature (i.e., lizardite and chrysotile) using two reference materials previously developed by Scicchitano *et al.* (2018a) at Mg# ~ 98 mole %. The new analytical protocol was then applied to constrain the physical–chemical conditions of fossil and modern peridotite hydration observed at depths of 20 m and 400 m in a site of active serpentinisation (Hole BA1B; Kelemen *et al.* 2018) in the Samail ophiolite (Oman). The mantle section of the Samail ophiolite shows evidence of at least three distinct hydrothermal events that occurred over a wide range of conditions and are likely to be recorded in the same sample (e.g., Noël *et al.* 2018). *In situ* measurement of oxygen isotopes in serpentine minerals has therefore the potential to unravel (i) the relative contribution of these episodes of water/rock interaction to the formation of serpentine, (ii) the physical and chemical conditions that favour low-*T* serpentinisation and (iii) the coupling between hydration and carbonation of peridotite in ophiolitic terrains.

Serpentine reference materials

Scicchitano *et al.* (2018a) provided a detailed characterisation of the chemical and oxygen isotope composition of samples Al06-44A, L3431 and C22908, which are therefore not repeated here. Recent studies by Tarling *et al.* (2018) and Andreani *et al.* (2008) highlighted that lizardite (Lz) has similar Raman spectra as polygonal and polyhedral serpentines (Pol.Srp), and hence cannot be distinguished by Raman spectroscopy. Consequently, it is not possible to rule

out that sample L3431 is either polygonal or polyhedral serpentine rather than lizardite. A second batch of sample Al06-44A was donated by Dr. J.A. Padròn-Navarta (University of Montpellier) in 2018 in order to increase its supply. This sample (hereafter UWSrp-1) was characterised at UW-Madison for comparison with Al06-44A analysed by Scicchitano *et al.* (2018a).

In order to extend the compositional range for accurate analysis of oxygen isotopes in serpentine minerals by SIMS, sixteen new serpentine samples were tested for chemical and isotopic homogeneity in order to determine their suitability as reference materials for oxygen isotope analysis by SIMS and a total of ten serpentine reference materials are described in Table 1.

Five new antigorite (Atg) reference materials (UWSrp-4 to UWSrp-8) were made from samples (A1, N7, 166405, BM66586 and 75-34, respectively) donated by Prof. B. Evans that were previously characterised for their major element composition and structural properties in a series of studies (Hess *et al.* 1952, Faust and Fahey 1962, Dietrich 1972, Uehara and Shirozu 1985, Uehara 1998, Evans *et al.* 2012). Additional analyses by Raman spectroscopy and EPMA were performed at UW-Madison to verify that the nature and chemical composition of the specimens were consistent with those reported in the literature.

Samples A1 (UWSrp-4) and N7 (UWSrp-5) are antigorite serpentinites corresponding to epidote amphibolite and glaucophane schist facies, respectively, from the Sangun (Sasaguri area, Japan) and Nagasaki (Nishisonogi area, Japan) metamorphic belts (Uehara and Shirozu 1985, Uehara and Kamata 1994, Uehara 1998). Both samples are composed of dark green antigorite lamellae with subordinate fine-grained magnetite and chromite (< 1% *v/v*, percentage by volume; Figure 1 and Figure S1). In sample UWSrp-5, antigorite occurs as both roundish and elongated grains. Sample 166405 (UWSrp-6) is a massive monomineralic antigorite serpentinite (< 1% *v/v* dusty fibres) from Caracas, Venezuela, characterised by a variable grain size with green antigorite up to ~ 1 mm in length (Figures 1 and S1; Hess *et al.* 1952, Evans *et al.* 2012). Sample BM66586 (UWSrp-7) came from the Mineralogical Collection of the Natural History Museum, London, and is a very pale green gem-quality antigorite from Afghanistan (Figures 1 and S1; Faust and Fahey 1962, Evans *et al.* 2012). The sample is very pure, and only sporadic apatite (< 1% *v/v*) is observed. Sample 75-34 (UWSrp-8) is from a vein of ferroantigorite associated with magnetite, sulfides and ilvaite cross-cutting serpentine in the Oberhalbstein Alps, Switzerland (Figures 1 and S1; Dietrich 1972, Evans *et al.* 2012). The source rock sample for this reference material is therefore heterogeneous, and careful mineral separation was necessary to handpick pure green antigorite grains. Sample GEM-2 (UWSrp-9) was purchased at a gem fair, and its geological provenance is unknown. The original hand sample consisted of two different antigorite generations – (i) roundish grains containing several small inclusions of heazlewoodite (Ni_3S_2) and abundant brucite (Brc), and (ii) relatively pure elongated grains with < 1% *v/v* magnetite (Mag) and brucite usually located towards the edge. UWSrp-9 consists of only the latter serpentine generation, handpicked for purity (Figures 1 and S1). Ten other serpentine samples were investigated but are either chemically or isotopically heterogeneous or consist of several serpentine generations that cannot be optically distinguished; hence, they are not further discussed in this study.

All antigorite reference materials developed here are chemically homogeneous within ± 1.04% *m/m* (per cent by mass) at most (2 standard deviation, 2*s*; Table 2), and no chemical differences were observed between roundish and elongated grains in sample UWSrp-5 within analytical precision. The major element compositions measured by EPMA at UW-Madison are comparable, within analytical precision, to those reported in previous studies of different pieces of each sample (Hess *et al.* 1952, Uehara and Shirozu 1985, Evans *et al.* 2012). The investigated samples, along with sample Al06-44A from Scicchitano *et al.* (2018a), cover most of the chemical compositional range observed in natural terrestrial serpentine minerals (Figure 2) in terms of SiO_2 (40.07–44.86% *m/m*), Al_2O_3 (0.21–3.30% *m/m*), MgO (30.49–42.74% *m/m*) and FeO(total) contents (0.38–15.80% *m/m*). In this study, the Mg number was calculated considering the Fe(total) – that is, Mg# = 100 × Mg/[Mg + Fe(total)], molar. Some serpentine contains significant Fe^{3+}; however, accurate $Fe^{3+}/\sum Fe$ is not routinely measured in natural samples. Consequently, the existing antigorite reference materials have Mg#s spanning over the range 77.5–99.5 mole %, which cover most of the compositional range commonly observed in natural terrestrial serpentine (Mg# ~ 78–99 mole %; Figure 2c; Evans *et al.* 2009, Evans *et al.* 2012, Mayhew and Ellison 2020). Nevertheless, accurate Fe^{3+} measurements for samples UWSrp-4 to UWSrp-8 and Al06-44A were previously published for different aliquots of the same samples (Evans *et al.* 2012, Debret *et al.* 2015) and we therefore estimate potential differences on matrix bias effects quantified using Mössbauer and Micro-X-ray absorption near-edge structure (μ-XANES) data and compare it with bias based on Fe(total) (see section *Relative bias due to Mg/Fe variation in antigorite*).

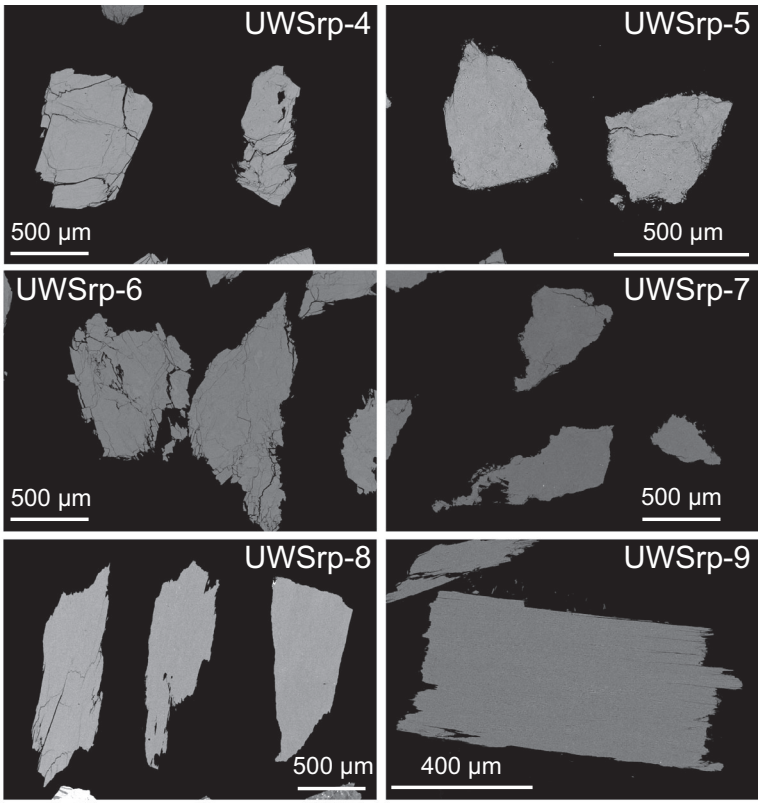

Figure 1. SEM-BSE images of new antigorite reference materials. (Srp = serpentine).

The Raman modes in the low-frequency (375–381, 683–689 and 1043–1052 cm^{-1}) and high-frequency regions (3667–3675 and 3698–3703 cm^{-1}) correspond to SiO and OH stretching vibrations, respectively, and are distinctive for the antigorite polymorph (Figure S2) (e.g., Rinaudo *et al.* 2003, Auzende *et al.* 2004, Reynard and Wunder 2006, Petriglieri *et al.* 2015, Tarling *et al.* 2018), in agreement with previous structural characterisations. The slight differences in the wavenumbers between different antigorite samples can be attributed to cation substitutions, particularly Fe and Al (Reynard and Wunder 2006), which vary by ~ 15% *m/m* and 3% *m/m*, respectively, among the different investigated samples.

Preparation of grain mounts

Serpentine reference materials

Serpentine samples were crushed, and four fractions (300–425 µm, 425–710 µm, 710–1400 µm and > 1400 µm) were checked for purity using a binocular reflected light microscope. Additional investigation by scanning electron microscopy (SEM) in secondary electron (SE) and backscattered electron (BSE) modes was performed to identify potential inclusions and chemical zoning. In order to determine the degree of oxygen isotopic homogeneity of the prospective serpentine reference materials, twenty grains of each sample from the 425- to 710-µm fraction were mounted in the central part of 25 mm epoxy discs (> 5 mm from the edge to avoid SIMS bias due to '*X-Y* effects'; e.g., Kita *et al.* 2009) along with known SIMS reference materials (UWQ-1 quartz, Kelly *et al.* 2007; UWC-3 calcite, Kozdon *et al.* 2009; Al06-44A, L3431 and C22908 serpentine, Scicchitano *et al.* 2018a). In order to flatten the surface and expose the grains, the epoxy discs were ground using a 6-µm fixed-diamond lapping pad on a spinning polishing wheel lubricated with a constant flow of water. They were then polished using 6 µm, 3 µm and 1 µm polycrystalline diamond suspensions on different low-nap polishing pads at a speed of 500 RPM and for no more than 1 minute for each grit to avoid the creation of surface relief that could adversely affect the quality of the SIMS data (e.g., Kita *et al.* 2009). Because of its fibrous nature, polishing of chrysotile C22908 was especially challenging for lamellae oriented with the elongation axis parallel to the surface of the mount, as previously shown by Scicchitano *et al.* (2018a). The flatness of the epoxy discs was checked using a ZYGO white-light interferometer at the Department of Materials

Table 1.
List of seven new serpentine reference materials investigated in this study, plus three from Scicchitano *et al.* (2018a)

RM	Sample ID	Serpentine	Mg# (mole %)*	$\delta^{18}O_{V\text{-}SMOW}$ (‰)**	Provenance	References
Al06-44A	Al06-44A	Atg	94.6	8.02	Cerro del Almirez massif (Spain)	1, 8
UWSrp-1	Al06-44A	Atg	94.8	8.38	Cerro del Almirez massif (Spain)	8
L3431	L3431	Lz/Pol.Srp.	98.3	5.32	Mineralogical Collection RSES (ANU)	1, 8
C22908	C22908	Ctl	98.1	4.66	Mineralogical Collection RSES (ANU)	1, 8
UWSrp-4	A1	Atg	91.9	7.52	Sangun metamorphic belt (Japan)	2, 3, 4, 8
UWSrp-5	N7	Atg	90.4	8.88	Nagasaki metamorphic belt (Japan)	2, 3, 4, 8
UWSrp-6	166405	Atg	97.8	5.59	Caracas (Venezuela)	4, 5, 8
UWSrp-7	BM66586	Atg	99.5	3.69	Natural History Museum (London)	4, 6, 8
UWSrp-8	75-34	Atg	77.5	6.45	Oberhalbstein Alps (Switzerland)	4, 7, 8
UWSrp-9	GEM-2	Atg	98.3	2.36	Unknown	8

1: Scicchitano *et al.* (2018a), 2: Uehara and Shirozu (1985), 3: Uehara (1998), 4: Evans *et al.* (2012), 5: Hess *et al.* (1952), 6: Faust and Fahey (1962), 7: Dietrich (1972), 8: this study.
RSES (ANU): Research School of Earth Sciences (Australian National University); UW-Madison: University of Wisconsin-Madison.
* Calculated using Fe(total).
** Recommended values used in this study (see Table 3 for details).

Science and Engineering (UW-Madison), and polishing relief is ≤ 3 μm. Mounts were carefully cleaned with ethanol and a concentrated Liquinox soap; they were then rinsed with distilled water and kept into a drying vacuum oven at 60 °C for 3 h before applying ~ 60-nm-thick gold coat.

Serpentinites from Hole BA1B (Samail ophiolite, Oman)

We investigated two serpentinites recovered during the ICDP Expedition 5057 from Site 5/Hole B (Hole BA1B, 22°52.874′ N, 58°42.035′ E) at depths of 20 m (core 7, section 2, interval 20–64 cm, hereafter BA1B-20) and 400 m (core 141, section 4, interval 0–58 cm, hereafter BA1B-400) from an area of active serpentinisation in the Samail ophiolite (Oman) cored in 2018 during the second phase of the Oman Drilling Project (Coggon *et al.* 2020, Senda *et al.* 2020, Kelemen *et al.* 2020a, b). The rock billets were first imaged with Raman spectroscopy at the University of Colorado-Boulder to identify different serpentine generations and polytypes as well as areas to be avoided during SIMS analysis (e.g., fine-grained intergrowths between serpentine and brucite). The samples were then imaged with the SEM in BSE mode at UW-Madison to identify chemical zoning in serpentine. Rock chips of ~ 2 mm × 2 mm × 3 mm containing the best target locations for SIMS analysis were then cut and mounted, along with grains of the SIMS reference material (antigorite Al06-44A ~ 300–500 μm in size), into the central part of 25-mm epoxy plugs. The polishing and cleaning procedures for the sample mounts were similar to those employed for the reference material mounts (see above, section *Serpentine reference materials*).

Analytical methods

Sample imaging

A Hitachi S3400 Variable Pressure Scanning Electron Microscope (VP-SEM) at the Department of Geoscience (UW-Madison) was used at high vacuum in BSE mode to (i) check the purity of the prospective serpentine reference materials by identifying inclusions and chemical zoning, and (ii) recognise different serpentine generations in the serpentinite samples from Hole BA1B to be analysed for oxygen isotope ratios by SIMS. Careful SEM imaging in both BSE and SE modes was also done after every SIMS session to check the location and features of each SIMS pit. This is particularly important for rock samples characterised by complex chemical zonation to verify the desired domains were analysed or whether SIMS analysis pits are located on mixed domains, fractures or other features that would make the measurement less reliable. SIMS analyses where the pit was located on mixed domains or fractures were discarded. Prior to SEM analysis, epoxy plugs were coated with carbon. Analytical conditions were usually as follows: accelerating voltage ~ 15 kV and working distance ~ 10 mm.

Major and minor element composition

Major and minor element quantitative analyses of serpentine were done with a CAMECA SXFive Field Emission Electron Microprobe at the Department of Geoscience (UW-Madison) using an accelerating voltage of 15 kV, a beam current of 10 nA and a 5-μm-diameter defocused beam. One to two analyses were done near every SIMS pit in the

Table 2.
Chemical compositions of new serpentine reference materials measured using EPMA. Values are means of 27 to 112 spot analyses on approximately twenty grains of each reference material

N. oxygen	14		14		14		14		14		14		14	
RM	UWSrp-1		UWSrp-4		UWSrp-5		UWSrp-6		UWSrp-7		UWSrp-8		UWSrp-9	
Serpentine	Atg		Atg		Atg		Atg		Atg		Atg		Atg	
	Mean (n = 50)	2s	Mean (n = 60)	2s	Mean (n = 112)	2s	Mean (n = 63)	2s	Mean (n = 63)	2s	Mean (n = 60)	2s	Mean (n = 27)	2s
% m/m														
SiO_2	41.52	0.87	43.27	0.61	42.52	0.67	43.60	0.67	44.86	0.40	40.07	0.60	43.67	1.04
TiO_2	< 0.03	0.03	< 0.03	< 0.03	< 0.03	< 0.03	< 0.03	< 0.03	< 0.03	< 0.03	< 0.03	< 0.03	< 0.03	< 0.03
Al_2O_3	2.89	0.41	0.61	0.30	1.04	0.32	0.75	0.28	0.21	0.07	2.09	0.15	0.81	0.48
Cr_2O_3	0.33	0.14	0.24	0.30	0.30	0.15	< 0.03	< 0.03	< 0.03	< 0.03	< 0.03	< 0.03	0.04	0.10
FeO(total)	3.79	0.53	5.99	0.37	6.99	0.36	1.64	0.23	0.38	< 0.08	15.80	0.60	1.33	0.30
MnO	0.09	0.08	0.09	< 0.07	0.16	< 0.07	< 0.07	< 0.07	< 0.07	< 0.07	0.10	< 0.07	< 0.07	< 0.07
MgO	38.41	0.65	38.00	0.64	36.83	0.88	41.75	0.71	42.74	0.62	30.49	0.62	41.94	0.84
CaO	< 0.02	0.02	< 0.02	< 0.02	< 0.02	0.06	< 0.02	< 0.02	0.02	0.18	< 0.02	< 0.02	< 0.02	< 0.02
Na_2O	< 0.04	< 0.04	< 0.04	< 0.04	< 0.04	< 0.04	< 0.04	< 0.04	< 0.04	< 0.04	< 0.04	< 0.04	< 0.04	< 0.04
NiO	0.18	0.22	0.24	< 0.09	0.27	< 0.09	0.18	< 0.09	< 0.09	< 0.09	< 0.09	< 0.09	< 0.09	< 0.09
H_2O (calculated)	12.79	< 1.00	12.84	< 1.00	12.71	< 1.00	13.05	< 1.00	13.21	< 1.00	12.21	< 1.00	13.06	< 1.00
Total	100.00	1.31	101.27	1.05	100.82	1.42	100.98	0.98	101.42	0.80	100.76	1.01	100.85	1.42
apfu														
Si	3.895	0.053	4.042	0.040	4.013	0.032	4.008	0.038	4.074	0.027	3.935	0.046	4.011	0.053
Ti	0.001	0.002	0.000	0.000	0.000	0.000	0.000	0.000	0.000	0.000	0.000	0.000	0.000	0.000
Al	0.320	0.046	0.067	0.033	0.116	0.036	0.082	0.031	0.023	0.007	0.242	0.017	0.088	0.052
Cr	0.024	0.010	0.018	0.022	0.023	0.011	0.000	0.000	0.000	0.000	0.000	0.000	0.003	0.008
Fe(total)	0.297	0.041	0.468	0.028	0.552	0.028	0.126	0.018	0.029	0.000	1.298	0.043	0.102	0.023
Mn	0.007	0.006	0.007	0.000	0.013	0.000	0.000	0.000	0.000	0.000	0.008	0.000	0.000	0.000
Mg	5.372	0.063	5.293	0.055	5.183	0.069	5.722	0.063	5.786	0.052	4.463	0.085	5.743	0.074
Ca	0.001	0.002	0.000	0.000	0.000	0.006	0.000	0.000	0.002	0.017	0.000	0.000	0.000	0.000
Na	0.001	0.006	0.000	0.000	0.000	0.000	0.000	0.000	0.000	0.000	0.000	0.000	0.000	0.000
Ni	0.017	0.024	0.018	0.000	0.021	0.000	0.013	0.000	0.000	0.000	0.000	0.000	0.000	0.000
Sum of cations	9.935	0.043	9.913	0.028	9.919	0.030	9.951	0.032	9.914	0.026	9.946	0.045	9.947	0.036
OH	8.00		8.00		8.00		8.00		8.00		8.00		8.00	
Mg# (mole %) *	94.8		91.9		90.4		97.8		99.5		77.5		98.3	
Mg# (mole %) *	97.0		93.2		91.8		98.4		99.6		80.0			

* Calculated using Fe(total).

** Mg# reported in the literature for different aliquots (Evans *et al.* (2012) for samples UWSrp-4 to UWSrp-8; Debret *et al.* (2015) for UWSrp-1).

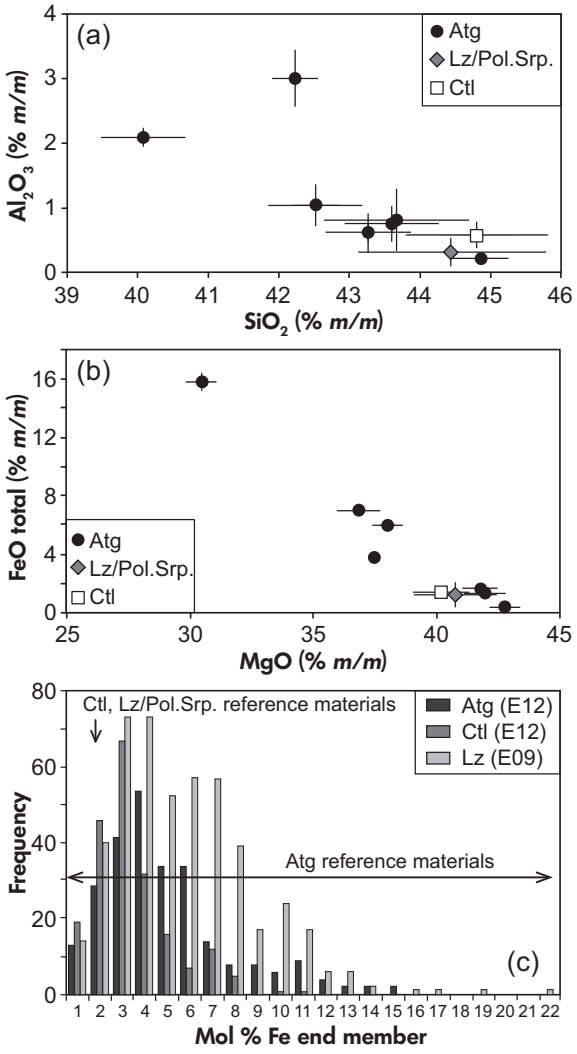

Figure 2. Diagrams showing the mean major element compositions of the nine serpentine reference materials in terms of (a) SiO_2 *versus* Al_2O_3, and (b) MgO *versus* FeO(total) (2*s*, Table 2). (c) Frequency histograms of total Fe in antigorite, chrysotile and lizardite from mantle-sourced metaperidotites (modified after E09 = Evans *et al.* 2009 and E12 = Evans *et al.* 2012) relative to the compositional range covered by the serpentine reference materials investigated in this study (black arrows). (Abbr.: Atg = antigorite, Ctl = chrysotile, Lz = lizardite, Pol.Srp = polygonal and polyhedral serpentine).

serpentinite samples from Hole BA1B in order to get an accurate chemical composition of the various domains analysed for oxygen isotope ratios. Prior to EPMA, epoxy mounts were coated with a 20-nm carbon layer (former gold coat was removed by dissolution following the procedure described in Jones *et al.* 2012). For each element, acquisition times were 10 s on peak and 10 s total on two background positions (5 s each). The following reference materials were used to calibrate each of the determined chemical elements: Kakanui hornblende USNM (Si, Ca; on LTAP and LPET analyser crystals, respectively), Burma Jadeite from the London National History Museum (Na and Al; TAP and LTAP crystals, respectively), Kilbourne Hole olivine and San Carlos olivine USNM (Mg; TAP crystal), Harvard University haematite (Fe; LLIF crystal), synthetic Mn_2SiO_4 (Mn; LLIF crystal), synthetic Ni_2SiO_4 (Ni; LLIF crystal), West Chester clinochlore Astimex (O; PC0 crystal), rutile or synthetic TiO_2 (Ti; LPET crystal), and Cr_2O_3 (Cr; LPET crystal). Matrix correction was done using the Armstrong/Love Scott method in the Probe for EPMA software (Armstrong 1988, Donovan *et al.* 2019), whereas background correction employed the mean atomic number (MAN) method (Donovan and Tingle 1996). Measurement of oxygen during EPMA improved the accuracy of the cation concentrations by up to ~ 2% *m/m*. The occurrence of time-dependent X-ray intensity (TDI) variations due to variable operating conditions during EPMA (e.g., Zhang *et al.* 2019) was tested with different beam currents (10 and 20 nA) and beam diameters (5 and 10 μm) and determined to be negligible in serpentine with the chosen analytical settings. All serpentine analyses were normalised to 18 (O + OH) according to the general formula $Mg_6Si_4O_{10}(OH)_8$. The calculated number of moles of Si was then used to estimate the approximate amount of H_2O in % *m/m*, assuming total iron as Fe^{2+} (see Table 2 for calculations). The calculated amount of H_2O would decrease by up to ~ 1% *m/m* if all ferric iron was assumed (*versus* all Fe^{2+}) in the structural formula.

Raman spectroscopy

An Aramis Horiba Jobin Yvon confocal Raman microscope at the Department of Material Sciences and Engineering (UW-Madison) was used to identify the polymorph type for the prospective serpentine reference materials. Raman spectra in serpentine reference materials were acquired directly on polished epoxy plugs using a 532 nm wavelength (green laser), 100 × objective, 600 lines mm^{-1} grating and a total acquisition time of 10 s resulting from five accumulations of 2 s each. The spectra were processed using the LabSpec 6 software in order to subtract the background and accurately assign wavelengths to the Raman peaks.

Raman imaging of the two serpentinite samples from Hole BA1B was conducted using a Horiba Jobin Yvon LabRAM HR Evolution confocal Raman microscope at the Department of Geological Sciences (University of Colorado-

Boulder). Hyperspectral Raman maps were collected using a 532 nm laser, 50 × objective, 600 line mm^{-1} grating and total acquisition time of 0.2–0.5 s per point depending on the map. Map processing was performed using LabSpec 6 software, including baseline subtraction and classical least-squares fitting based on end members defined by averaging multiple spectra within the map data set.

Oxygen isotope analysis by laser fluorination

Bulk oxygen isotope measurements of the serpentine reference materials were performed with a 32 W CO_2 laser fluorination system coupled with a triple-collecting Finnigan/MAT 251 mass spectrometer at the Stable Isotope Laboratory, UW-Madison (Valley *et al.* 1995), using an airlock to minimise sample crosstalk and partial reaction prior to analysis (e.g., Spicuzza *et al.* 1998). Approximately 10 to 100 mg (depending on the initial availability) of each serpentine sample (425–710 μm fraction) was handpicked under a binocular reflected light microscope in order to choose inclusion-free and unaltered grains for laser fluorination analysis. The selected grains were ground to a fine powder and three to eight aliquots of ~ 2 mg each per sample were loaded in 2-mm-diameter holes located in individual nickel sample holders, which were then kept in a drying oven prior to introduction into the airlock chamber (for details on instrumental design and analytical procedures, see Valley *et al.* 1995, Spicuzza *et al.* 1998). The garnet reference material (UWG-2, Valley *et al.* 1995) was analysed six times at the start of, and twice during, each of five daily sessions. Raw values were corrected using the mean measured value for UWG-2 compared with the recommended value of 5.80‰ V-SMOW for UWG-2 on each day (Valley *et al.* 1995). The mean correction was -0.03‰, and daily precision averaged ± 0.10‰ (2*s*).

Oxygen isotope analysis by SIMS

In situ oxygen isotope analyses of serpentine were performed with a CAMECA IMS-1280 large-radius multi-collector secondary ion mass spectrometer at the WiscSIMS Laboratory (UW-Madison) during eight measurement sessions from August 2018 to June 2020. Serpentine in the samples from Hole BA1B was analysed during the session in June 2019. A primary beam of $^{133}Cs^+$ ions with ~ 2 nA intensity and accelerating potential of +10 kV (20 kV impact energy) were focused to ~ 10 μm diameter beam size at the surface of the sample (Kita *et al.* 2009, 2010). Epoxy mounts were coated with ~ 60-nm layer of gold to enhance conductivity. Additionally, a normal-incidence electron-flood gun (-10 kV) was used to focus electrons at 0 energy over the sputtering site (~ 60 μm × 100 μm oval area) to compensate for the build-up of positive charge typical of analyses employing a Cs^+ primary ion beam (e.g., Kita *et al.* 2009, 2010). The contrast aperture, entrance slit, field aperture, energy slit and exit slit were set to 400 μm diameter, 120 μm width, 4000 μm × 4000 μm, 40 eV width at low-energy peak and 240 μm width, respectively (e.g., Kita *et al.* 2010). Simultaneous analysis of $^{16}O^-$, $^{18}O^-$ and $^{16}O^1H^-$ ions was done using three Faraday Cup (FC) detectors; count rates in serpentine were on the order of ~ 2.3–3.8 × 10^9 cps, ~ 4.7–7.6 × 10^6 cps and ~ 6.5 × 10^7 to 1.5 × 10^8 cps, respectively. Each analysis lasted ~ 3.5 min including 10 s of presputtering necessary to remove the gold coat, 120 s of automated centring of the secondary ions during which the secondary ion signal stabilises and 80 s of data collection resulting from an integration of twenty cycles of 4 s each (Kita *et al.* 2009). Bias, drift and spot-to-spot precision were monitored by bracketing every 10–20 unknown analyses with eight analyses of the reference material located in the same grain mount.

Data treatment

Estimation and correction of bias for serpentine reference materials

By convention, the measured oxygen isotope ratios ($^{18}O/^{16}O$) are expressed using the δ-notation as permil deviation relative to Vienna-Standard Mean Ocean Water (V-SMOW) (Kita *et al.* 2009, Hoefs 2018), with ($^{18}O/^{16}O$) = 0.00200520 (Baertschi 1976).

Measured values of ($^{18}O/^{16}O$) by SIMS are biased relative to true ratios during sample sputtering as well as transmission and detection of the secondary ion beam. Instrumental mass fractionation (IMF) is expressed by a fractionation factor, $\alpha^{18}O_{SIMS}$ (e.g., Deloule *et al.* 1991, Kita *et al.* 2009):

$$\alpha^{18}O_{SIMS} = \frac{1+\delta^{18}O_{RAW}/1000}{1+\delta^{18}O_{LF}/1000} \quad (1)$$

where $\delta^{18}O_{RAW}$ is the $\delta^{18}O$ value of a reference material measured by SIMS, and $\delta^{18}O_{LF}$ is the oxygen isotope value of the same reference material determined by laser fluorination that is accepted as the true value and tied to the V-SMOW scale. Because $\alpha^{18}O_{SIMS}$ is generally close to unity for oxygen isotopes on Earth, it is closely approximated using δ-notation in permil referred to as 'bias' (Kita *et al.* 2009):

$$bias = (\alpha^{18}O_{SIMS} - 1) \times 1000 \quad (2)$$

Bias of individual minerals and their solid solution can change slightly within or between measurement sessions, though the relative differences between two minerals will remain constant within a single week-long session. Therefore, we define the difference in instrumental bias for a mineral with variable solid solution relative to that determined for a specific reference material (typically the running reference material, RS) as bias* (‰):

$$\text{bias}* = \left(\frac{\alpha^{18}O_{SIMS}}{\alpha^{18}O_{SIMS-RS}} - 1\right) \times 1000 \quad (3)$$

In this study, we used the antigorite reference material Al06-44A as the normalising serpentine reference material in sessions S4, S6 and S7 (Table S2). UWQ-1 quartz, UWC-3 calcite and SCO-ANU olivine (Scicchitano *et al.* 2018b) were used as running reference materials in sessions S1 to S5 and S7, which aimed to test the isotopic homogeneity of the prospective serpentine reference materials or potential grain orientation effects in serpentine.

Estimation and correction of bias for unknowns

The suite of reference materials reported here allows evaluation of the matrix effects of Fe-Mg substitution in antigorite for Mg# = 77.5 to 99.5 mole %. We did not find pure suites of chemically and isotopically homogenous lizardite and chrysotile samples that could be pursued as SIMS reference materials to span the full range Mg# ~ 78 to 100 mole %. Accordingly, all seven antigorite reference materials (Al06-44A and UWSrp-4 to UWSrp-9) were analysed at the beginning of each measurement session in order to determine a calibration curve, which allowed for the correction of every serpentine analysis in the rock samples for bias*(*x*), the extent of bias due to variation in chemical composition, *x*, relative to the normalising reference material (see Equation (5) in section *Relative bias due to Mg/Fe variation in antigorite* for details). Additionally, the lizardite (L3431) and chrysotile (C22908) reference materials were also analysed at the beginning of each measurement session to estimate the relative bias (bias*) attributable to differences in crystal structures between serpentine polymorphs. For measurement sessions that used UWC-3 calcite as a running reference material, we calculated the relative bias (bias*) between UWC-3 and Al06-44A and the bias* (*x*) against Al06-44A (Table S2).

The final corrected $\delta^{18}O$ values expressed on the V-SMOW scale for each unknown were calculated as follows:

$$\delta^{18}O_{V-SMOW} = \left(\frac{1+\delta^{18}O_{RAW}/1000}{1+bias/1000} - 1\right) \times 1000 \quad (4)$$

where $\delta^{18}O_{RAW}$ and bias are as defined above (see Table S3a, for details on calculations).

Calculation of precision and accuracy on oxygen isotope measurements

In the WiscSIMS Lab, the analytical precision of an individual analysis was assessed by the spot-to-spot precision of the bracketing reference material (2*s*, typically $n = 8$, Table S2) rather than by the measurement repeatability of twenty cycles for a given spot (i.e., 2 SE, standard error of the mean; Kita *et al.* 2011). The isotopic homogeneity of the prospective serpentine reference materials was estimated by comparing the spot-to-spot precision (2*s*) of multiple analyses in approximately twenty grains with the precision of the bracketing reference materials Al06-44A, UWQ-1 or UWC-3 that are homogenous within ± 0.1–0.5‰ (Tables S1 and S2).

The reported accuracy (2*s*) on the $\delta^{18}O$ values of serpentine from Hole BA1B samples (Table S3a) is the quadratic sum of the standard error of the individual SIMS analysis (i.e., measurement repeatability, 2SE, of each SIMS spot); standard error of the bracketing reference material; and standard errors of the laser fluorination values of (i) antigorite Al06-44A (2SE = 0.08‰, Table 3), (ii) garnet UWG-2 (2SE = 0.01‰, Valley *et al.* 1995), (iii) quartz NBS-28 (2SE = 0.09‰, Valley *et al.* 1995), and (iv) lizardite L3431 (2SE = 0.10‰, Table 3) or chrysotile C22908 (2SE = 0.02‰, Table 3) depending on the nature of the analysed serpentine polymorph, and the precision of the matrix bias calibration (2RMSE = 0.51‰ for the June 2019 session; Table S2).

Oxygen isotopes in serpentine reference materials

Laser fluorination and gas-source mass spectrometry

The serpentine reference materials as well as the San Carlos olivine (SCO-ANU) were analysed for oxygen isotope ratio by laser fluorination and gas-source mass spectrometry of 1–2 mg samples at the Stable Isotope Laboratory, UW-Madison (Table 3). Aliquots of the new prospective serpentine reference materials and sample UWSrp-1 were analysed three to eight times/each, and the previously characterised serpentine reference materials Al06-44A, L3431 and C22908 as well as San Carlos olivine SCO-ANU were analysed two to four times each.

Most serpentine samples had a precision ≤ 0.3‰ (2*s*), whereas one sample (UWSrp-6) had a precision of ~ 0.4‰ (2*s*) (Table 3). The new laser fluorination data acquired at UW-Madison on samples Al06-44A (8.02 ± 0.16‰, 2*s*, *n* = 4), L3431 (5.32 ± 0.20‰, 2*s*, *n* = 4) and C22908 (4.66 ± 0.04‰, *n* = 3) are used throughout this paper for consistency.

Secondary ion mass spectrometry

SIMS measurements of oxygen isotope ratios in the serpentine reference materials were performed during eight measurement sessions (Tables S1 and S2). The first three sessions (S1 to S3 in Table S2) aimed to determine the isotopic homogeneity at the microscale of the new serpentine samples (UWSrp-4 to UWSrp-9), whereas sessions S4 to S7 (Table S2) aimed to evaluate (i) the extent of relative bias between antigorite samples with variable Mg#s, (ii) relative bias between different serpentine polymorphs and (iii) any possible grain orientation effects. The last session (S8 in Table S2) aimed to compare UWSrp-1 with Al06-44A.

Grain orientation effects: Channelling and tunnelling effects can cause the measured oxygen isotope ratio by SIMS to vary for some minerals according to the orientation of the target's crystal structure to the primary and secondary beams. Orientation effects have been documented in a few oxide minerals, but chrysotile is the only silicate to show an effect of many that have been tested (Huberty *et al.* 2010, Kita *et al.* 2011, Scicchitano *et al.* 2018a). The possible occurrence and extent of orientation effects in serpentine were investigated with a CAMECA IMS-1280 secondary ion mass spectrometer by analysing different orientations (i.e., fibre/grain elongation parallel and perpendicular to the surface of the mount) of Ctl C22908 and Atg UWSrp-9. An orientation effect of up to ~ 1‰ was observed in chrysotile, whereas no significant variability in $\delta^{18}O$ between different orientations was detected in the antigorite (Figure 3).

The extent of orientation effect in chrysotile varied over the three measurement sessions, potentially due to the analysis of different chrysotile grains in the mounts (Figure 3). In particular, the orientation when fibres are parallel to the surface of the mount showed comparable raw $\delta^{18}O$ values in December 2018 and higher raw $\delta^{18}O$ values in the two subsequent sessions (by ~ 0.5–1.0‰), relative to the orientation when fibres are perpendicular to the surface of the mount (Figure 3). We excluded the possibility that the lower $\delta^{18}O$ values might be due to the occurrence of epoxy in the analysed domains because no epoxy was detected during SEM-BSE imaging and secondary ion yields in the two orientations were comparable (Table S2). During the session in June 2019, we tested whether the different orientation of the chrysotile fibres relative to the incoming primary ion beam could be responsible for such variability by rotating the same epoxy mount of 90° (Figure S3). Nevertheless, a similar extent of orientation effects was observed between the two orientations of chrysotile (Figure 3). The same mount was analysed in January 2019 with a third orientation relative to the Cs^+ primary beam (Figure S3), and a comparable extent of orientation effect was observed (Figure 3; Table S2).

Scicchitano *et al.* (2018a) also observed up to 1‰ difference in orientation effects in the Ctl C22908 using SHRIMP SI and SHRIMP II instruments. In particular, comparable $\delta^{18}O$ values between the two orientations were obtained with SHRIMP SI, whereas an offset of ~ 1‰ (with higher values in the fibres with elongation axis parallel to the surface of the mount) was observed with SHRIMP II in the same mount. This difference was attributed to variations in the instrument design and potentially to differences in the analytical settings between the two instruments that may have suppressed orientation effects on SHRIMP II. Interestingly, the magnitude of orientation effects detected with SHRIMP SI is comparable to that detected with the CAMECA IMS-1280, despite the two instruments having different primary ion beam incidence angles (e.g., Huberty *et al.* 2010).

To the best of our knowledge, chrysotile is the only silicate in which orientation effects have been described, whereas they are consistently observed during oxygen isotope analysis of magnetite and haematite (Huberty *et al.* 2010); U-Pb isotope analysis of rutile (Taylor *et al.* 2012) and baddeleyite (Wingate and Compston 2000, Schmitt *et al.* 2010); S isotope analysis in sphalerite and galena; and Fe isotopes in magnetite (Kozdon *et al.* 2010, Kita *et al.* 2011).

The reason for the variation in orientation effects in chrysotile observed from session to session in this study is unclear. Analytical settings were kept constant over the different sessions and are an unlikely cause of this discrepancy. The nature of orientation effects observed here differs from those that have been reported in single crystals of other minerals, in part because the phyllosilicate layers are rolled in fibres of chrysotile that are < 100 nm in outer diameter and ≥ 4 nm in inner diameter (Evans *et al.* 2013). Thus, each 10-μm SIMS pit on chrysotile targets several fibres that have highly variable crystallographic orientation. Additionally, the core of the fibres may be empty or filled by amorphous matter (Evans *et al.* 2013). This may cause the variability of orientation effects

observed from session to session by both CAMECA and SHRIMP instruments. Similar variability in orientation effects from session to session has not been observed in other minerals (Huberty *et al.* 2010, Kozdon *et al.* 2010, Kita *et al.* 2011). Additional studies are necessary to determine the cause(s) of this variation. The maximum extent of orientation effects recorded in chrysotile is ~ 1‰ and therefore is considered to be the limitation on the precision and accuracy of analyses of this polymorph.

Isotopic homogeneity of new serpentine reference materials: Overall, analysis of the majority of the new antigorite reference materials yielded mean precisions ranging between ± 0.2 and 0.5‰ (2*s*), comparable to that of the commonly used reference materials at WiscSIMS that were analysed in the same sessions: UWQ-1 quartz (± 0.3 to 0.5‰, 2*s*), UWC-3 calcite (± 0.1 to 0.4‰, 2*s*) and Al06-44A antigorite (± 0.3 to 0.5‰, 2*s*) (Table S1). Chrysotile C22908 (precision commonly ± 0.2 to 0.5‰ and occasionally up to ± 0.8‰, 2*s*, for the fibres with elongation axis parallel to the surface of the mount; see above section *Grain orientation effects*) and lizardite L3431 (± 0.2 to 0.5‰, 2*s*) were analysed during the same measurement sessions (Tables S1 and S2). Slightly less precise were the antigorite samples UWSrp-4 (± 0.3 to 0.6‰, 2*s*) and UWSrp-5 (± 0.4 to 0.7‰, 2*s*) (Tables S1 and S2). The precision in some of these serpentine reference materials (e.g., UWSrp-4 and UWSrp-5) is larger than that commonly achieved for other minerals at the WiscSIMS Laboratory for a 10 μm beam size (0.2–0.3‰, 2*s*; e.g., Kita *et al.* 2009, Tenner *et al.* 2017) as well as in the other serpentine reference materials, demonstrating that UWSrp-4 and UWSrp-5 are not perfectly homogeneous in oxygen isotope ratios. However, UWSrp-4 and UWSrp-5 are still useful as reference materials. We did not detect drift at a level of 0.3‰ for any of the SIMS sessions. The bias for each reference material varied by as much as ~ 3.8‰ between different sessions (Tables S1 and S2), but within a single measurement session, the extent of bias was comparable between the various serpentine polymorphs (2.8–6.6‰ for Atg with Mg# = 77.5–99.5; 1.4–4.0‰ for Lz/Pol.Srp.; 0.9–5.2‰ for Ctl) (Tables S1 and S2). The bias with SHRIMP instruments from previous studies (Scicchitano, unpublished results) was larger compared with the results determined with the CAMECA IMS-1280 in this study. In particular, bias values for SHRIMP SI and SHRIMP II varied as follows: 10.1–16.0‰ and 6.4–7.8‰ for the Atg Al06-44A (*versus* 2.8–6.5‰ with the CAMECA IMS-1280), 9.3–10.4‰ for the Lz/Pol.Srp. L3431 (no data were acquired with SHRIMP II), and 10.3–11.8‰ and 7.1–8.0‰ for the Ctl C22908 (Scicchitano, unpublished results). The bias for UWSrp-1 was comparable to that of Al06-44A within analytical precision (Table S2).

Relative bias due to Mg/Fe variation in antigorite: A systematic relationship between relative bias and Mg#, bias*(*x*), was observed for the antigorite reference materials over three different measurement sessions from December 2018 to June 2019. This relationship can be described by a second-order polynomial (Figure 4):

$$bias*(x) = ax^2 + bx + c \quad (5)$$

where *x* is Mg# (mole %) of the antigorite reference materials determined by EPMA; a, b and c are the parameters of the regression determined at the start of each measurement session from the results of the seven reference materials (Table S2). In the investigated compositional range, the largest difference in matrix bias effect relative to Al06-44A – that is, ~ -1.8‰ – was observed for the Fe-rich sample UWSrp-8 with Mg# of ~ 78 (Figure 4). Uncertainty of bias*(*x*) is estimated as the deviation from the best-fit curve and was ~ 0.5–1.0‰ (2*s*) over the three measurement sessions. Calibration curves were also determined using Mg#s of antigorite reference materials calculated on the basis of the measured Fe^{2+}/Fe^{3+} ratios published in Evans *et al.* (2012), for samples UWSrp-4 to UWSrp-8, and Debret *et al.* (2015), for sample Al06-44A. These calibration curves were compared with those determined using Mg#s derived from Fe(total). The extent of matrix bias correction calculated using the two different sets of calibration curves differs only by ~ 0.3‰ at most. Consequently, given this difference is within the typical analytical precision, the lack of accurate $Fe^{3+}/\sum Fe$ ratios for most natural serpentine is not a significant limitation to the accuracy of SIMS analyses.

No clear correlation between bias*(*x*) and major element chemistry for Al_2O_3 (0.21–3.30% *m/m*) and OH/O (3.2–3.4 E–02) was observed in the investigated compositional range (Figure 5).

Even though the systematic relationship between Mg# and relative bias can be similar if analytical settings are kept constant, some inter-session variability is observed and accurate analysis requires the construction of a calibration curve at the beginning of every measurement session. Furthermore, relative bias should be extrapolated beyond the compositional range covered by the reference materials only with great care and the degree of nonlinearity should be evaluated before interpolations over large intervals in major element composition.

Table 3.
Oxygen isotope values of serpentine reference materials and San Carlos olivine (SCO-ANU) investigated in this study determined by laser fluorination and gas-source mass spectrometry of ~ 2 mg aliquots using an airlock sample chamber to prevent pre-fluorination (Spicuzza *et al.* 1998)

RM	Serpentine	This study					Scicchitano *et al.* (2018a)				
		$\delta^{18}O_{V\text{-}SMOW}$ (‰)	Mean $\delta^{18}O_{V\text{-}SMOW}$ (‰)	2*s* (‰)	2SE (‰)	Comment	$\delta^{18}O_{V\text{-}SMOW}$ (‰)	Mean $\delta^{18}O_{V\text{-}SMOW}$ (‰)	2*s* (‰)	2SE (‰)	Laboratory
Al06-44A	Atg	7.91	8.02	0.16	0.08	Day 3	8.24	8.22	0.07	0.05	UNIL
		8.06					8.19				
		8.09				Day 6	8.36	8.39	0.08	0.06	U. Sc. Tec.,
		8.03					8.42				China (Hefei)
UWSrp-1	Atg	8.42	8.38	0.06	0.04	Day 1					
		8.36									
		8.37									
L3431	Lz/Pol.Srp.	5.45	5.32	0.20	0.10	Day 3	5.06	5.26	0.57	0.40	U. Sc. Tec.,
		5.21					5.46				China (Hefei)
		5.35				Day 6					
		5.28									
C22908	Ctl	4.67	4.66	0.04	0.02	Day 3	4.35	4.37	0.04	0.03	U. Sc. Tec.,
		4.64				Day 6	4.38				China (Hefei)
		4.68									
UWSrp-4	Atg	7.35	7.52	0.24	0.12	Day 1					
		7.62									
		7.59				Day 3					
		7.52									
UWSrp-5	Atg	8.89	8.88	0.09	0.05	Day 1					
		8.83									
		8.92									
UWSrp-6	Atg	5.37	5.59	0.42	0.19	Day 1					
		5.72									
		5.84									
		5.37				Day 3					
		5.63									
UWSrp-7	Atg	3.53	3.69	0.32	0.18	Day 1					
		3.68									
		3.85									
UWSrp-8	Atg	6.50	6.45	0.19	0.11	Day 2					
		6.51									
		6.34									

Table 3 (continued).
Oxygen isotope values of serpentine reference materials and San Carlos olivine (SCO-ANU) investigated in this study determined by laser fluorination and gas-source mass spectrometry of ~ 2 mg aliquots using an airlock sample chamber to prevent pre-fluorination (Spicuzza *et al.* 1998)

RM	Serpentine	This study				Sicchitano *et al.* (2018a)			
		$\delta^{18}O_{V\text{-}SMOW}$ (‰)	Mean $\delta^{18}O_{V\text{-}SMOW}$ (‰)	2*s* (‰)	2SE (‰)	Comment	$\delta^{18}O_{V\text{-}SMOW}$ (‰)	Mean $\delta^{18}O_{V\text{-}SMOW}$ (‰)	2*s* (‰)	2SE (‰)	Laboratory
UWSrp-9	Atg	2.37	2.36	0.31	0.11	Day 1					
		2.40									
		2.39				Day 3					
		2.46									
		2.49				Day 4					
		2.24									
		2.49									
		2.04									
SCO-ANU	Ol	5.57	5.55	0.07	0.05	Day 5					
		5.52									

Atg: antigorite, Lz: lizardite, Ctl: chrysotile, Pol.Srp: polygonal and polyhedral serpentine, Ol: olivine

Relative bias between different serpentine polymorphs: Given that lizardite L3431 and chrysotile C22908 have different Mg/Fe ratios (Mg# = 98.3 and 98.1, respectively; Table S2) relative to the normalising antigorite reference material Al06-44A (Mg# = 94.6; Table 1), the observed difference in bias may result from a combination of variable chemical compositions and crystal structures. In order to disentangle these two effects and evaluate the extent of bias due to differences in crystal structures, the measured $\delta^{18}O$ values of lizardite and chrysotile reference materials were corrected according to Equation (4), assuming that the relation between bias*(x)

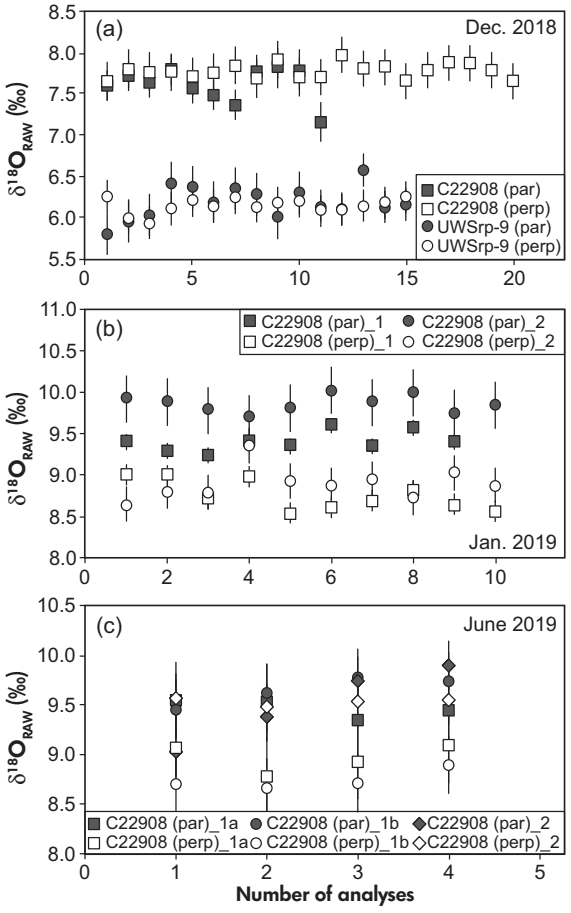

Figure 3. Raw $\delta^{18}O$ values in two different orientations (i.e., parallel and perpendicular to the surface of the mount) of chrysotile C22908 and antigorite UWSrp-9 grains over three measurement sessions, showing grain orientation effects up to ~ 1‰ in chrysotile. No orientation effects were detected in antigorite. (c) Rotation of the same mount by 90° gave comparable $\delta^{18}O$ values within analytical precision (C22908_1a *versus* C22908_1b). See text for more details.

and Mg# (Equation 5) is the same for all serpentine polymorphs (Table S2). The offset between the corrected $\delta^{18}O$ value relative to antigorite Al06-44A and the oxygen isotope ratio determined by laser fluorination is the extent of bias attributed to differences in crystal structures at that Mg# composition between various serpentine polymorphs. A bias of ~ -0.5 to -1.0‰ was calculated for lizardite L3431 *versus* antigorite Al06-44A during the three measurement sessions (Figure 6), and the difference in bias calibrated for each session is therefore included in the bias*(*x*) term for all unknown lizardite analyses (Table S3a). A bias of ~ -0.1 to -1.2‰ and ~ -0.7 to -1.0‰ was calculated for chrysotile C22908 with the fibre elongation parallel and perpendicular, respectively, to the surface of the mount (Figure 6, Table S2). Given that this is within the precision of chrysotile analyses due to orientation effects, it was not included in the bias*(*x*) term for unknown chrysotile analyses (Table S3a).

A limited number of studies have investigated the possible occurrence of differences in the SIMS bias between different polymorphs. In studies of coesite and quartz (Schulze *et al.* 2003), no difference in the bias was observed.

Serpentinisation at Hole BA1B, Samail ophiolite (Sultanate of Oman)

Geological background and previous studies

The Samail ophiolite in northern Oman and eastern United Arab Emirates is the largest (~ 10,000 km^2), best-exposed and least-deformed ophiolite complex in the world (Hacker *et al.* 1996, Boudier *et al.* 2010, Kelemen *et al.* 2011, Streit *et al.* 2012, Früh-Green *et al.* 2018). For these reasons, it has been intensely studied over the past 40 years to better understand the formation and alteration of the oceanic lithosphere at fast-spreading ridge centres and after obduction (e.g., Gregory and Taylor 1981, Godard *et al.* 2003, Nasir *et al.* 2007, Streit *et al.* 2012, Rioux *et al.* 2012, 2013, Falk *et al.* 2016) as well as the efficiency of *in situ* CO_2 sequestration in peridotite through mineral carbonation reactions (e.g., Kelemen and Matter 2008, Kelemen *et al.* 2011, Noël *et al.* 2018). The Oman Drilling Project recently recovered ~ 3000 m of core from critical sections within the dyke–gabbro transition, the foliated and layered gabbros, the crust–mantle transition, the boundary between the ophiolite and the underlying metamorphic sole and Hawasina Group, including 1000 m of core from zones undergoing active serpentinisation (e.g., Teagle *et al.* 2018).

The mantle section of the Samail ophiolite (~ 8–12 km thick) is affected by high degrees of serpentinisation (typically 30–60%, reaching 100% in large areas) and carbonation that is more localised. The alteration is ascribed to at least three distinct hydrothermal events spanning a large range of time, environment and temperature: (i) seafloor serpentinisation before obduction (i.e., likely between ~ 97 and 95 Ma, Hacker *et al.* 1996, Rioux *et al.* 2013) at T = 130–400 °C (e.g., Dewandel *et al.* 2003, Boudier *et al.* 2010, Streit *et al.* 2012); (ii) carbonation of the mantle wedge during obduction (i.e., between ~ 95 and 78 Ma, Hacker *et al.* 1996) at T = 80–130 °C due to interaction with metasediment-derived fluids (e.g., Falk and Kelemen 2015); and (iii) present-day low-T (< 50 °C) weathering and interaction with meteoric water (e.g., Barnes *et al.* 1978, Neal and Stanger 1984, 1985, Stanger 1985, Streit *et al.* 2012, Miller *et al.* 2016). Evidence for peridotite carbonation recorded at the microscale and attributable to these three main hydrothermal events has recently been described by Noël *et al.* (2018) who performed the first *in situ* stable isotope (O, C) study by SIMS in carbonate veins cross-cutting serpentinised harzburgites in the Wadi Dima area of the Samail ophiolite.

The Oman Drilling Project 'Batin Alteration' (BA) cored and rotary drill sites ('BA1B', 'Site 9/Hole A' or 'BA3A', and 'Site 10/Hole A' or 'BA4A') are closely spaced in Wadi Lawayni located in the large Wadi Tayin massif in the mantle section of the ophiolite (e.g., Kelemen *et al.* 2020a,b). Preliminary observations of the BA drill cores highlighted the occurrence of several mutually cross-cutting (and therefore presumed cogenetic) veins consisting of 'waxy' fine-grained serpentine (often observed at contact between serpentinised peridotite and altered gabbroic dykes), carbonate and serpentine + carbonate (Kelemen *et al.* 2018). Dating of the carbonate veins using ^{14}C (≤ 8% fraction modern carbon) yields ages of 20 to 52 ky, suggesting that some of the 'waxy' serpentine may also be young (Kelemen *et al.* 2020a). The abundance of these young veins decreases down-hole, and carbonate veins are only observed in the upper 100 m of the cores; similarly, oxidation of the matrix with abundant formation of Fe-oxy-hydroxides is pervasive in the upper 30 m of all holes and decreases down-hole (Kelemen *et al.* 2018). This correlation between abundance of young veins and matrix alteration with depth as well as the occurrence of highly alkaline and reduced fluids sampled in the boreholes ('type-I' Mg^{2+}-HCO_3^--rich waters with pH ~ 8–9; 'type-II' Ca^{2+}-$(OH)^-$-rich waters with pH ~ 10–11 and mixtures of the two; e.g., Barnes and O'Neil 1969, Miller *et al.* 2016, Kelemen *et al.* 2020a) suggests that carbonation and serpentinisation of peridotite could be active, near-surface processes at BA sites (Kelemen *et al.* 2018).

Site BA1B samples 400 m of extensively serpentinised peridotite (~ 150 m upper dunite and ~ 250 m lower harzburgite with > 80% alteration), cross-cut by several gabbroic and pyroxenite dykes. In this study, two serpentinite

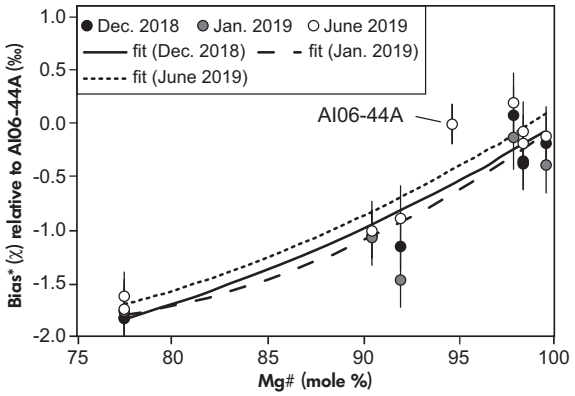

Figure 4. Relationship between Mg# [100 × Mg/(Mg + Fe), molar] and bias*(x) due to matrix effects during oxygen isotope analysis of antigorite reference materials with the CAMECA IMS-1280 secondary ion mass spectrometer over three measurement sessions. Bias*(x) is the difference in bias for an antigorite RM relative to the normalising antigorite reference material, Al06-44A.

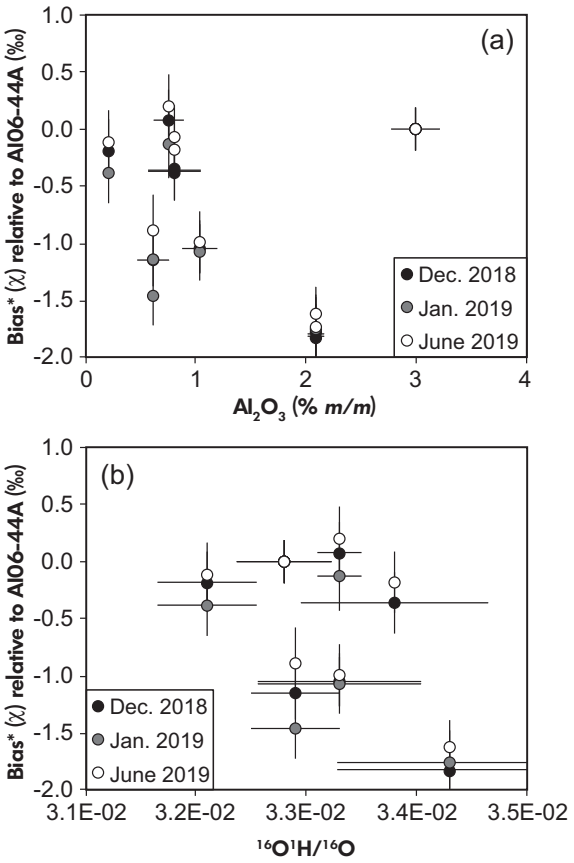

Figure 5. Diagrams showing bias*(x) in antigorite reference materials. There is no clear correlation between bias and (a) Al_2O_3, or (b) $^{16}O^1H/^{16}O$.

samples recovered from the BA1B drill core at depths of 20 m (sample BA1B-20) and 400 m (sample BA1B-400) were investigated in detail by SEM-BSE imaging, EPMA major chemical element, Raman and oxygen isotope microanalysis in serpentine minerals. This allowed for characterising and constraining the origin and petrogenesis of multiple serpentine veins within the context of the three different hydrothermal alteration events proposed for the Samail ophiolite and particularly the physical and chemical conditions of modern *versus* fossil serpentinisation.

Sample description

BA1B-400: In sample BA1B-400, collected at 400 m depth at the bottom of the BA1B cored borehole, the primary igneous mineral assemblage is partially preserved and consists of minor relicts of olivine with rare pyroxene and Cr-spinel (Figure 7a, b). Relict olivine is often observed in the core of mesh textures surrounded by lizardite ± chrysotile (polymorphs determined by Raman spectroscopy, Figures 7a, S4a), while orthopyroxene (with clinopyroxene exsolution lamellae) is replaced by pseudomorphic bastite (Figure 7a). Mesh and bastite textures, typical of seafloor alteration under static conditions (e.g., Andreani *et al.* 2007), are surrounded by hourglass textures characterised by lizardite ± chrysotile sometimes intergrown with fine-grained brucite. In addition, several veins consisting of serpentine + magnetite ± brucite occur at the original grain boundaries or in mesh textures (Figure 7a, b). These veins (V-1) have variable widths, from a few μm up to ~ 200 μm, and the largest ones consist of lizardite + magnetite ± brucite (V-1a) that are no longer constrained to former grain boundaries and are cross-cut by chrysotile veinlets < 50 μm in width (V-1b; Figure 7b). Major element chemical compositions of the various serpentine generations from sample BA1B-400 are shown in Figure S5 and Table S3b.

BA1B-20: Sample BA1B-20 is a completely serpentinised sample from 20 metres depth where the only relicts of the primary igneous mineral assemblage are rare Cr-spinels. The igneous texture of the protolith is still preserved locally in mesh textures that, in contrast to sample BA1B-400, do not contain any olivine relict; the contact between mesh core and mesh rims is sharp (Figure 7c), and it is therefore difficult to ascertain which of the two formed first (e.g., O'Hanley 1996). As in sample BA1B-400, serpentine + magnetite ± brucite veins (V-1) follow grain boundaries or are located in mesh textures and show no preferred orientation (Figure 7c). In addition to mesh textures, the matrix of the rock also consists of a serpentine + magnetite assemblage

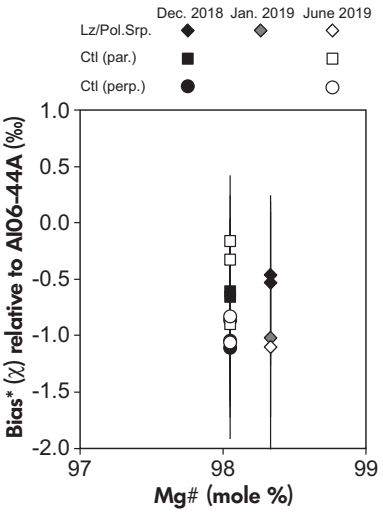

Figure 6. Diagram showing the extent of bias due to differences in crystal structure between antigorite and other serpentine reference materials (i.e., Ctl C22908 and Lz/Pol.Srp. L3431). Needle orientations: par. = parallel, perp. = perpendicular to sample surface.

(Figure 7d), which sometimes seems to surround mesh textures. Raman spectroscopy allowed the identification of several chrysotile generations as well as antigorite in the matrix of sample BA1B-20 (Figure S4b). Fine-grained chrysotile veins (V-2) up to ~ 200 μm in width cross-cut chrysotile in the matrix as well as in V-1 veins (Figure 7d, e). V-2 veins are cross-cut, in turn, by later chrysotile veins (V-3) with variable widths (from ~ 50 to 500 μm in width). Raman spectroscopy and SEM-BSE imaging show that the largest V-3 veins consist of up to seven different chrysotile generations and are characterised by banding parallel to the edges of the vein (Figure 7e, f; Figure S4b). Single chrysotile bands in BSE images have a thickness variable from ~ 1 to ~ 250 μm (Figure 7e, f). EPMA highlighted that the largest V-3 veins have a symmetric zoning in silica and alumina contents as well as Mg/Fe ratios that vary from the edges towards the centre of the vein (Figure 8). V-3 veins may have formed by a repeated crack-seal mechanism along the same vein (e.g., Ramsay 1980, Andreani *et al.* 2007), and they form a network of veins mutually cross-cutting at an angle of ~ 90° (Figure 7f). Major element chemical compositions of all serpentine generations from sample BA1B-20 are shown in Figure S5 and Table S3b.

In situ oxygen isotope measurements in serpentine from Hole BA1B

A total of 523 analyses were performed by SIMS in serpentine from samples BA1B-20 and BA1B-400 (Table S3a). The antigorite Al06-44A was used as the running (and normalising) reference material, and all antigorite reference materials were analysed at the start of the measurement session to calibrate the relative bias over the compositional range Mg# = 77.5–99.5. Additionally, both lizardite (L3431) and chrysotile (C22908) reference materials were analysed at the start of the measurement session to calibrate bias relative to the antigorite Al06-44A, as explained in section *Relative bias between different serpentine polymorphs*. Measured $\delta^{18}O$ values of serpentine in samples BA1B-20 and BA1B-400 were corrected according to Equation (4) and reported relative to the V-SMOW scale (Table S3a).

BA1B-400: Mesh, hourglass and lizardite V-1a veins from sample BA1B-400 have comparable $\delta^{18}O$ values ranging between 4.4–5.6‰, 3.9–7.0‰ and 3.9–7.3‰, respectively (Figure 9; Table S3a). Later chrysotile V-1b veins are characterised by higher oxygen isotope ratios ($\delta^{18}O$ = 6.7–8.5‰; Figure 9; Table S3). No correlation was observed between $\delta^{18}O$ and [MgO + FeO(total)] for any of the analysed serpentine generations (Figure S6).

BA1B-20: Mesh cores in sample BA1B-20 are higher in $\delta^{18}O$ relative to mesh rims ($\delta^{18}O$ = 7.2–9.3‰ *versus* 6.0–7.3‰, respectively; Figure 9; Table S3a). Comparable $\delta^{18}O$ values were measured in 'matrix Ctl 1' ($\delta^{18}O$ = 7.0–7.8‰), 'matrix Ctl 2' ($\delta^{18}O$ = 6.6–8.5‰), antigorite ($\delta^{18}O$ = 6.8–7.3‰) and V-2 veins ($\delta^{18}O$ = 6.8–7.9‰) (Figure 9; Table S3a). Both the lowest and the highest $\delta^{18}O$ values in sample BA1B-20 are recorded, respectively, at the edges (~ 4.6‰) and centre (~ 11.0‰) of late V-3 veins (Figures 7d, e, 8, 9). The symmetric chemical and oxygen isotope zoning (up to ~ 6.5‰) observed in the largest V-3 veins (Figure 8) may suggest that chrysotile generations become progressively younger towards the centre of the veins.

The systematic variation in $\delta^{18}O$ values observed within and between the two investigated samples can be summarised in three stages: (i) 'Stage I', $\delta^{18}O$ values increase by ~ 3‰ on average from serpentine in the matrix at 400 m depth to serpentine in the matrix at 20 m depth; (ii) 'Stage II', $\delta^{18}O$ values decrease by ~ 3‰ on average from serpentine in the matrix to serpentine at the edge of V-3 veins at 20 m depth; and (iii) 'Stage III', $\delta^{18}O$ values increase by up to ~ 6.5‰ from the edge towards the core of V-3 veins (Figure 9). Interestingly, oxygen isotope compositions as low as those recorded in the matrix serpentine at 400 m depth are not observed in any of the matrix serpentine at 20 m depth. A possible interpretation of these observations is discussed below.

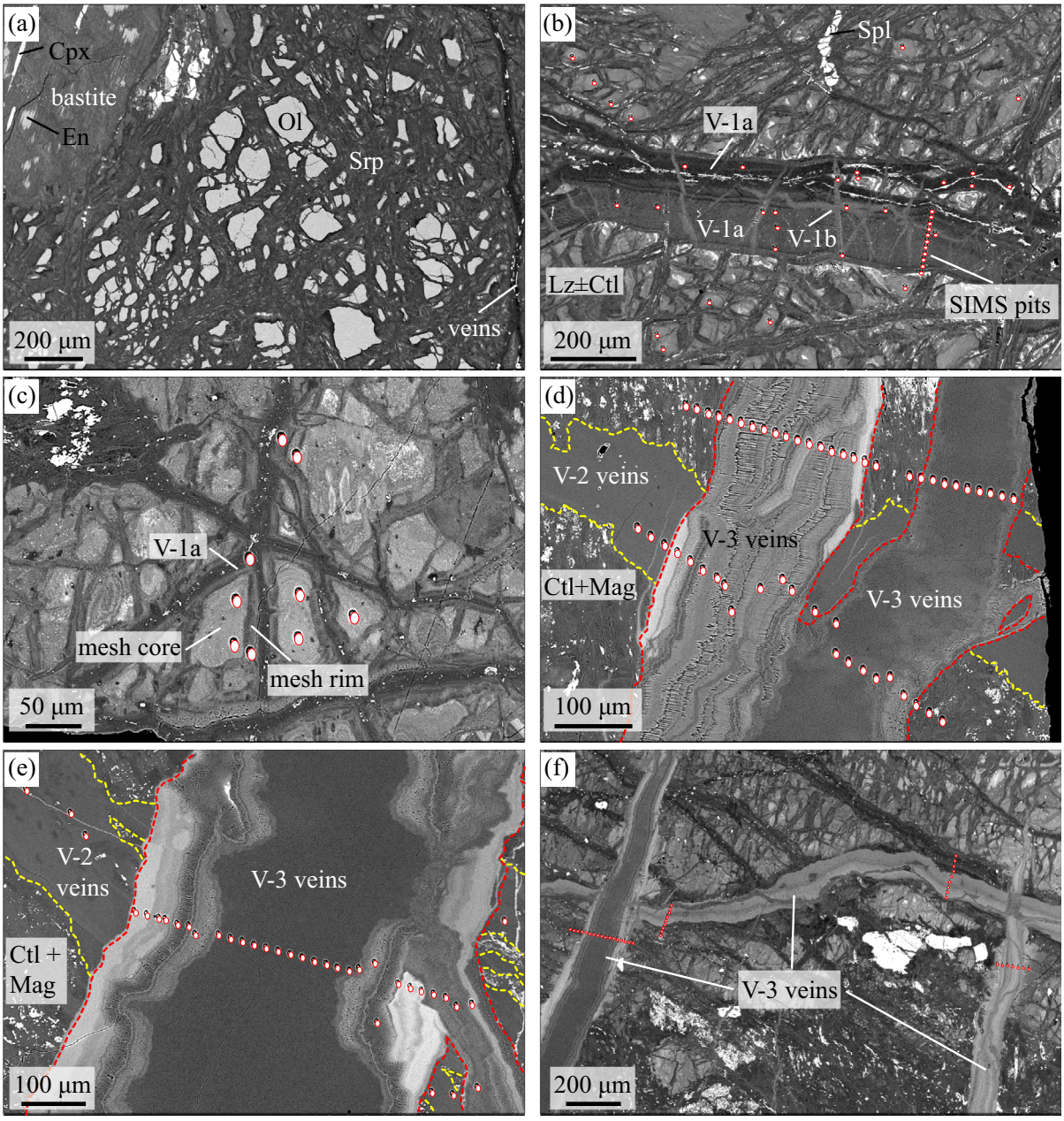

Figure 7. SEM-BSE images of representative textures in samples BA1B-400 (a, b) and BA1B-20 (c–f). (a) Relic olivine and pyroxene (En: enstatite, Cpx: clinopyroxene) in mesh and bastite textures, respectively, and serpentine + magnetite ± brucite veins (sample BA1B-400). (b) Lizardite + magnetite ± brucite V-1a veins cross-cut by chrysotile V-1b veins in hourglass serpentine matrix with relict Cr-spinel (sample BA1B-400). (c) Mesh textures in sample BA1B-20. (d, e) Fine-grained serpentine veins (V-2) cross-cutting serpentine + magnetite matrix in sample BA1B-20; later banded V-3 veins cross-cut V-2 veins. V-3 veins are chemically and isotopically zoned. (f) V-3 veins forming a network of veins mutually cross-cutting at an angle of ~ 90° (sample BA1B-20). The positions of SIMS pits (white dots) are shown in Figures 7b–f. [Colour figure can be viewed at wileyonlinelibrary.com]

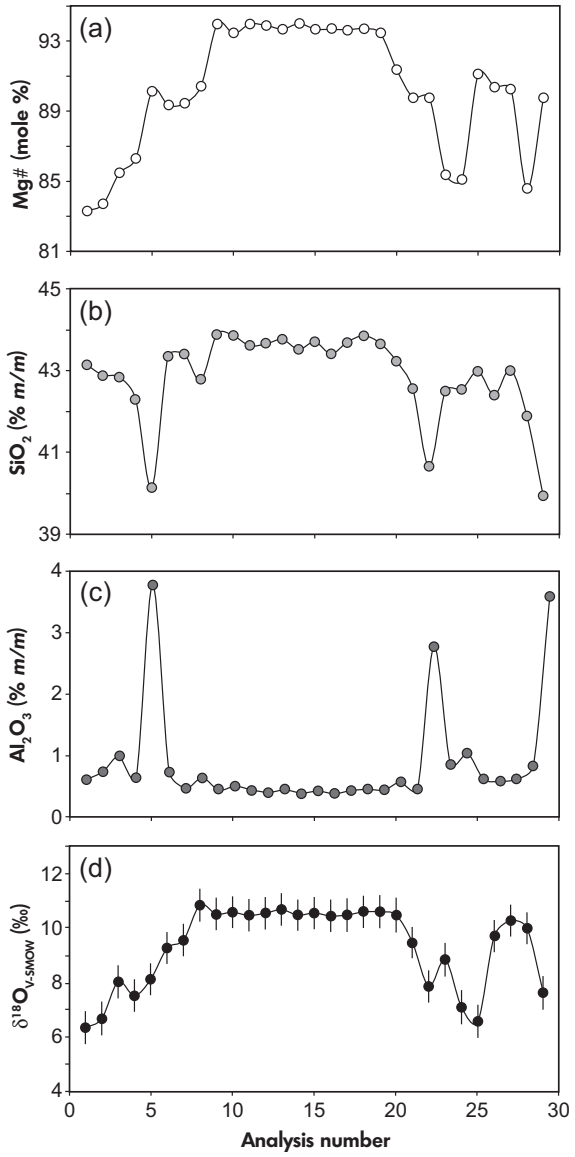

Figure 8. Symmetric, edge-to-edge chemical (a–c) and oxygen isotope zoning (d) measured in banded V-3 vein from Figure 7e (sample BA1B-20).

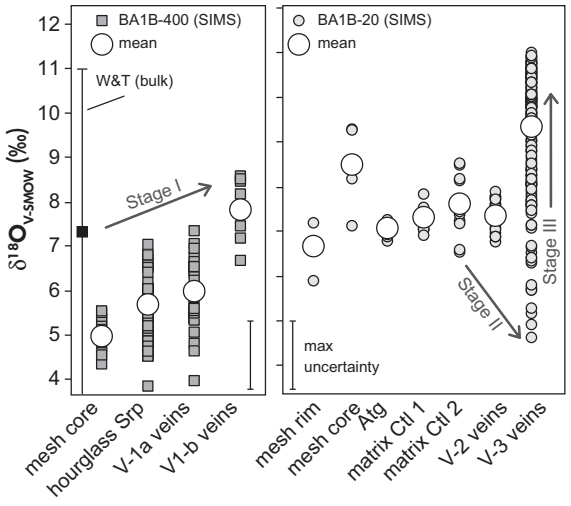

Figure 9. Summary of oxygen isotope measurements by SIMS performed in different serpentine generations from samples BA1B-400 and BA1B-20. The mean (black square) and total range in $\delta^{18}O$ values measured in serpentinites using bulk techniques are also shown (after Wenner and Taylor 1973, 1974). The systematic variability in $\delta^{18}O$ values observed between the two samples can be summarised in three different stages (I, II, III).

Discussion

The dependence of equilibrium isotope fractionation on temperature and chemical composition has important geological applications for stable isotopes as geothermometers and tracers of fluid flow provided that isotope fractionation factors between mineral–mineral and mineral–fluid pairs are known and that isotopic equilibrium is achieved and preserved (e.g., Hoefs 2018). Several studies have calibrated the fractionation of oxygen isotopes in serpentine minerals using empirical (e.g., Wenner and Taylor 1971, Früh-Green *et al.* 1996), theoretical (e.g., Savin and Lee 1988, Zheng 1993) or experimental methodologies (e.g., Saccocia *et al.* 2009) and can therefore be used to calculate the temperature of serpentinisation (if the $\delta^{18}O$ of the fluid is known) or the oxygen isotope composition of the serpentinising fluid (if the equilibrium temperature is known). It is important to note that the various calibrations of the serpentine–water system agree within ± 2‰ at temperatures of 250 to 450 °C, while a large discrepancy (> 4‰ and up to ~ 20‰) is observed when empirical and experimental calibrations are extrapolated to temperatures < 250 °C (Figure 10).

Extrapolation of the experimental calibration by Saccocia *et al.* (2009) to $T < 250$ °C yields temperatures that are ~ 100 °C higher relative to those calculated by extrapolating the empirical calibration by Früh-Green *et al.* (1996) and would suggest a lack of serpentine formation during low-*T* modern water/rock interaction at Hole BA1B (Table S3b). Given that modern interaction with groundwater is inferred at BA sites, we will discuss our results using the empirical calibration by Früh-Green *et al.* (1996) extrapolated at $T < 250$ °C because it predicts alteration temperatures that are consistent with water temperatures < 50 °C measured in boreholes at BA sites (Nothaft *et al.* in prep.) as well as in groundwater in adjacent pre-existing wells and

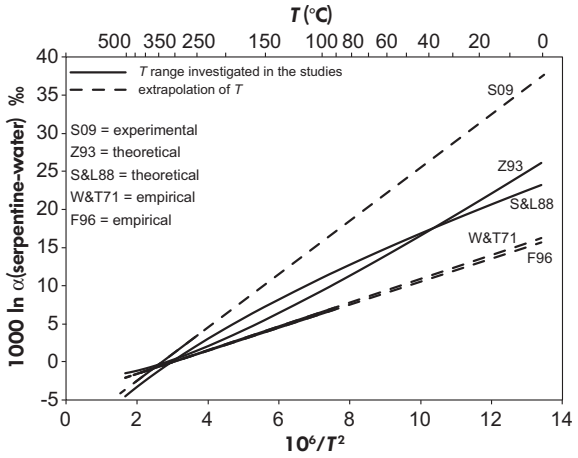

Figure 10. Plot showing the calibrations for serpentine–water oxygen isotope fractionation available in the literature (W&T71 = Wenner and Taylor 1971; S&L88 = Savin and Lee 1988; Z93 = Zheng 1993; F96 = Früh-Green *et al.* 1996; S09 = Saccocia *et al.* 2009). Solid lines are for temperatures investigated in the different studies, while dashed lines are our extrapolations to lower temperatures assuming linearity. See text for more details.

alkaline springs in the Samail ophiolite (e.g., Neal and Stanger 1985, Falk *et al.* 2016, Miller *et al.* 2016).

Variations in serpentinising temperature(s) and fluid(s) at Hole BA1B: The systematic variation in $\delta^{18}O$ values observed between the two investigated samples (stages I to III) can be explained with four different models that differ only in the interpretation of 'Stage I', whereas the interpretations of 'Stages II and III' are similar for all models. Our interpretations for the three different stages are summarised below.

- Seafloor serpentinisation. 'Stage I' can be the result of four different scenarios that all involve interaction with seawater. In fact, the mesh and hourglass textures observed in sample BA1B-400 have oxygen isotope compositions ($\delta^{18}O$ = 3.9–7.0‰) that are consistent with seafloor alteration at T ~ 124 °C to 112 °C ($\delta^{18}O$ seawater = 0‰) or ~ 189 °C to 171 °C ($\delta^{18}O$ seawater = +2.5‰). Higher serpentine $\delta^{18}O$ values measured in chrysotile V-1b veins in the same sample ($\delta^{18}O$ = 6.7–8.5‰) and in the matrix serpentine of sample BA1B-20 ($\delta^{18}O$ = 6.0–9.3‰) can result from (1) cooling to ~ 62 °C if we consider a fluid dominated scenario where the alteration involves seawater with a constant $\delta^{18}O$ value (~ 0‰) during ocean-floor alteration (Figure 11a; Table S3b); (2) an increase in $\delta^{18}O$ value of circulating seawater at relatively constant temperature (Figure 11b) due to interaction with the oceanic crust (e.g., Putlitz *et al.* 2001); (3) a progressive increase in the water/rock ratio (and therefore extent of equilibration with seawater) from incipient to advanced serpentinisation during seafloor alteration (e.g., Rouméjon *et al.* 2018); or (4) modern water/rock interaction with groundwater having a $\delta^{18}O$ value of at least -2.5‰ at serpentinisation temperatures of ~ 31 to 67 °C (Figure 11c). The latter scenario would be consistent with current water temperatures and $\delta^{18}O$ values of ~ 35 to 45 °C and -2.6‰ and -2.2‰, respectively, that were measured in the nearby Hole BA1A (Nothaft *et al.* in prep.) as well as with previous clumped isotope thermometry on carbonate veins in serpentinised peridotites (< ~ 50 °C; e.g., Streit *et al.* 2012). It could also explain at a first approximation the relation between the $\delta^{18}O$ variations in the two samples with the present-day erosional surface. To summarise, 'Stage I' could have occurred entirely as seafloor serpentinisation (scenarios 1 to 3; Figure 11a-b) or it could have started in an ocean-floor setting followed by a first influx of meteoric water at low-T in continental setting (scenario 4; Figure 11c).

- Infiltration of meteoric water. Influx of low $\delta^{18}O$ groundwater during 'Stage II' is the most likely scenario able to explain the decrease by ~ 3‰ on average from serpentine in the matrix of sample BA1B-20 to serpentine at the edge of the latest V-3 veins (Figure 9). The water in equilibrium with serpentine at the edge of V-3 veins (serpentine $\delta^{18}O$ = 4.6‰) would have an oxygen isotope composition of ~ -7‰ at T = 32 °C (Figures 11a–d), which is the mean modern recharge temperature at shallower depth (< 50 m) in the peridotite aquifers of Oman (Paukert Vankeuren *et al.* 2019). Despite $\delta^{18}O$ values of modern groundwater and alkaline springs in the Samail ophiolite vary from ~ -3.0‰ to ~ +2.5‰ (e.g., Neal and Stanger 1985, Falk *et al.* 2016, Miller *et al.* 2016), speleothem evidence shows that fossil groundwater could have been significantly lower in $\delta^{18}O$. Water fluid inclusions extracted from stalagmites from the Hoti Cave (northern Oman) dating to the last interglacial period (~ 125 ka) record $\delta^{18}O$ values of ~ -7.8‰ to -4.2‰, and mean $\delta^{18}O$ values in speleothems were ~ 6‰ lower during the last interglacial period than they are today (Fleitmann *et al.* 2011, Nicholson *et al.* 2020).

Increase in serpentine $\delta^{18}O$ values of ~ 6.5‰ from the edge to the core of V-3 veins ('Stage III'; Figure 9) is most likely explained by a shift to higher $\delta^{18}O$ values of

groundwater due to water/rock interaction or mixing with more positive $\delta^{18}O$ fluids (Figure 11d). The chemical zoning recorded by chrysotile in V-3 veins also suggests a variation in the chemistry of the fluid circulating through the veins. Interestingly, the variation in serpentine $\delta^{18}O$ values in V-3 veins is comparable to the increase by ~ 6‰ on average $\delta^{18}O$ values measured in speleothems from the Hoti Cave in northern Oman (Fleitmann *et al.* 2011). It is unlikely that the oxygen isotope zoning measured in V-3 veins is due solely to cooling because it would require a decrease in temperature by ~ 50 °C (at constant $\delta^{18}O$ fluid). This would be inconsistent with the observation that the older groundwater (> 60 y old) sampled at depths> 50 m in the peridotite aquifer has noble gas temperatures (NGTs) that are only ~ 7 °C lower (or ~ 25 °C on average) relative to the younger groundwater (4–40 y old) sampled at depths

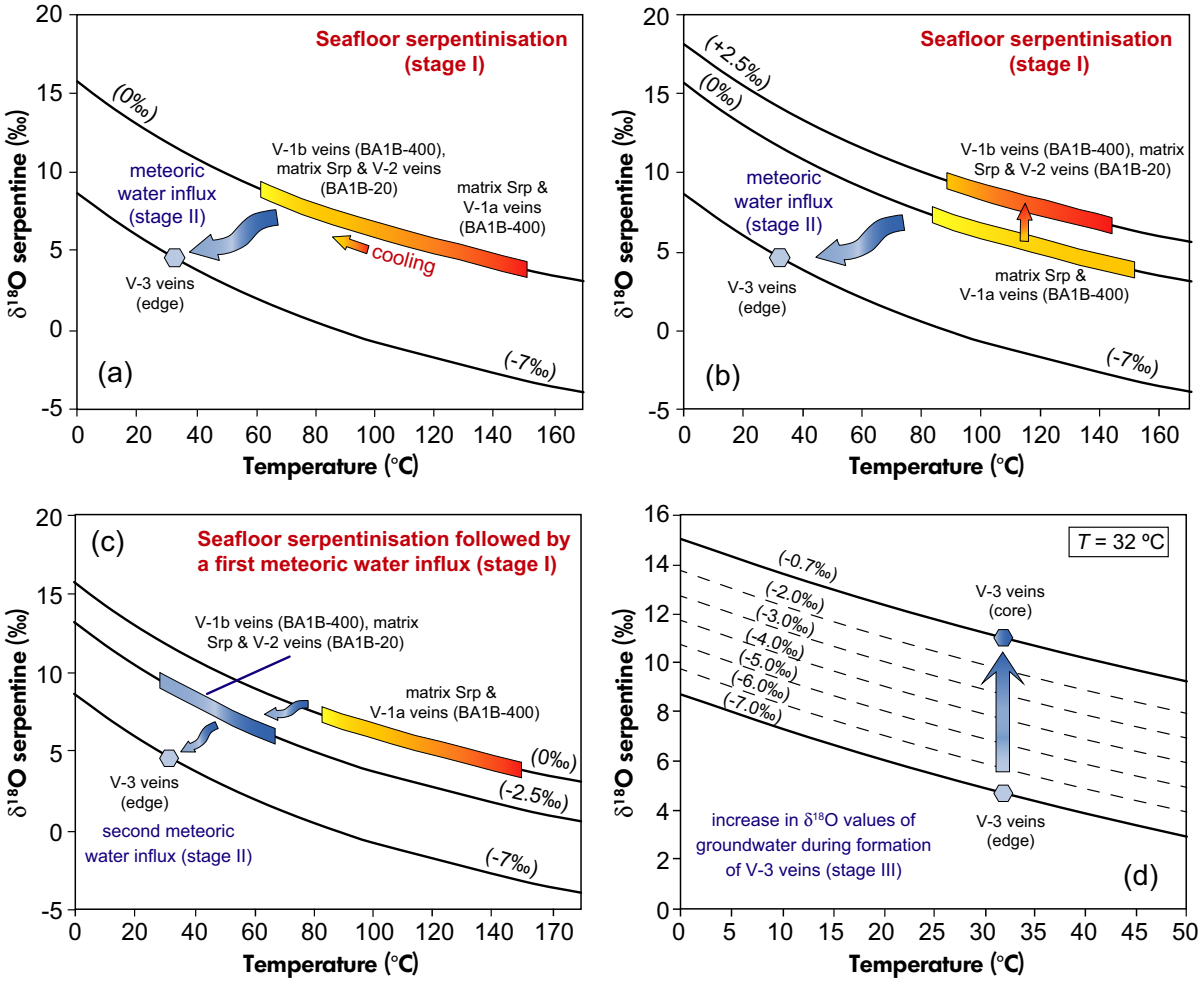

Figure 11. Models for thermal and fluid history of serpentinisation from samples BA1B-400 and BA1B-20. Temperatures are based on measured $\delta^{18}O$ values in serpentine (serpentine–water oxygen isotope fractionation factors after Früh-Green *et al.* 1996). 'Stage I' is interpreted as the result of (a) cooling during seafloor alteration assuming a constant $\delta^{18}O$ value of 0‰ for seawater, (b) increase in the $\delta^{18}O$ value of seawater from 0‰ to +2.5‰ during ocean-floor alteration due to interaction with the oceanic crust at a relatively constant temperature and (c) seafloor alteration followed by a first influx of meteoric water with a $\delta^{18}O$ value of at least -2.5‰ at $T \leq$ ~ 50 °C. (a–c) The most likely scenario for 'Stage II' is the influx of meteoric water with a $\delta^{18}O$ value of ~ -7‰ at T = 32 °C that is the mean modern recharge temperature at shallow depth (< 50 m) in peridotite aquifers in Oman. Alternatively, a $\delta^{18}O$ value of at least ~ -5‰ is required for the formation of chrysotile at the edges of V-3 veins at $T \leq$ 50 °C. (d) The most likely scenario for 'Stage III' is the shift of groundwater $\delta^{18}O$ to more positive values as a result of water/rock interaction or mixing with higher $\delta^{18}O$ meteoric fluids. See text for more details. [Colour figure can be viewed at wileyonlinelibrary.com]

< 50 m in the peridotite aquifer (NGTs = 30 to 33 °C) (Paukert Vankeuren *et al.* 2019).

Need for future studies: In order to realise the full potential of *in situ* oxygen isotope measurement to decipher the complex history of serpentinites and to correctly attribute different serpentine generations to the three hydrothermal events recorded in Hole BA1B in the Samail ophiolite, it is crucial to (i) determine a more accurate calibration of the oxygen isotope fractionation between serpentine and water at $T < 250$ °C due to the current uncertainty associated with the extrapolation of the experimental and empirical calibrations at low temperatures; (ii) analyse more samples located at intermediate depths in the drill core BA1B as well as in nearby holes at BA sites in order to understand how the variation in $\delta^{18}O$ values measured in serpentine minerals relates to the modern hydrology of the aquifer; and (iii) couple *in situ* measurement of oxygen isotopes in serpentine and co-precipitated minerals (e.g., magnetite, carbonates, talc, brucite and quartz) observed in different localities of the Samail ophiolite in order to better constrain the temperatures of serpentinisation and potentially build an empirical calibration of the serpentine–water oxygen isotope fractionation at low temperature. These further studies will have implications for correctly understanding the physical and chemical conditions of serpentinisation not only in the Samail ophiolite but also in other tectonic settings world-wide.

Conclusions

In situ measurement of oxygen isotopes by SIMS in serpentine minerals can be accurately done over the full compositional range normally found in nature (Mg# = 77.5–99.5 mole %) with a precision of ≤ 0.5‰ (2*s*) in antigorite and lizardite, and ~ 1‰ in chrysotile due to the occurrence of grain orientation effects. Matrix bias effects up to ~ 1.8‰ were observed in antigorite reference materials with variable Mg/Fe ratio, demonstrating the need of matrix-matched reference materials for ensuring accuracy of analyses in unknown samples.

Application of the new analytical protocol allowed accurate measurements of systematic variation in $\delta^{18}O$ values of up to ~ 7‰ at the micrometre scale in two serpentinite samples from the active serpentinisation site BA1B in the Samail ophiolite, which would have been concealed by bulk analyses. We suggest that both seafloor alteration and modern water/rock interaction are recorded at Hole BA1B by the serpentine in the matrix of sample BA1B-400 and by the latest V-3 veins in sample BA1B-20, respectively.

Acknowledgements

We thank Bernard Evans for donating samples (A1, N7, 166405, BM66586 and 75-34) and José Alberto Padròn-Navarta for providing sample Al06-44A. Noriko Kita, Kouki Kitajima and Ian Orland are thanked for assistance and training in the WiscSIMS Lab; Brian Hess for assistance with sample preparation, John Fournelle, Will Nachlas and Bil Schneider for assistance with EPMA and SEM imaging and Ben Linzmeier for assistance with QGIS. We also thank the Oman Drilling Project (PIs Peter Kelemen, Juerg Matter and Damon Teagle), which provided crucial access to water and rock samples from the active serpentinisation BA sites. This study was supported by the U.S. Department of Energy, Office of Science, Office of Basic Energy Sciences under Award Number DE-FG02-93ER14389, the Rock-Powered Life NASA Astrobiology Institute (NNA15BB02A) and NASA Astrobiology Institute Director's Discretionary Fund. WiscSIMS is supported by the U.S. National Science Foundation (EAR-1658823) and the University of Wisconsin-Madison. We thank thorough reviews from two anonymous reviewers and Regina Mertz-Kraus for editorial handling. None of the authors have any conflict of interest to declare.

Data Availability Statement

All data are available within the paper or are available from the authors on request.

References

Alt J.C., Garrido C.J., Shanks W.C., Turchyn A., Padrón-Navarta J.A., López S.-V., Gómez Pugnaire M.T. and Marchesi C. (2012)
Recycling of water, carbon, and sulfur during subduction of serpentinites: A stable isotope study of Cerro del Almirez, Spain. **Earth and Planetary Science Letters**, 327–328, 50–60.

Andreani M., Grauby O., Baronnet A. and Muñoz M. (2008)
Occurrence, composition and growth of polyhedral serpentine. **European Journal of Mineralogy**, 20, 159–171.

Andreani M., Mével C., Boullier A.M. and Escartín J. (2007)
Dynamic control on serpentine crystallization in veins: Constraints on hydration processes in oceanic peridotites. **Geochemistry, Geophysics and Geosystems**, 8, 1–24.

references

Armstrong J.T. (1988)
Quantitative analysis of silicate and oxide materials: Comparison of Monte Carlo, ZAF, and Phi-Rho-Z procedures. In: Newbury D.E. (ed.), Proceedings of the Microbeam Analysis Society, 239–246.

Auzende A.L., Daniel I., Reynard B., Lemaire C. and Guyot F. (2004)
High-pressure behaviour of serpentine minerals: A Raman spectroscopic study. Physics and Chemistry of Minerals, 31, 269–277.

Baertschi P. (1976)
Absolute ^{18}O content of standard mean ocean water. Earth and Planetary Science Letters, 31, 341–344.

Barnes J.D., Beltrando M., Lee C.T.A., Cisneros M., Loewy S. and Chin E. (2014)
Geochemistry of Alpine serpentinites from rifting to subduction: A view across paleogeographic domains and metamorphic grade. Chemical Geology, 389, 29–47.

Barnes I. and O'Neil J.R. (1969)
The relationship between fluids in some fresh Alpine-type ultramafics and possible modern serpentinization, western United States. Geological Society of America Bulletin, 80, 1947–1960.

Barnes I., O'Neil J.R. and Trescases J.J. (1978)
Present day serpentinization in New Caledonia, Oman and Yugoslavia. Geochimica et Cosmochimica Acta, 42, 144–145.

Bindeman I. (2008)
Oxygen isotopes in mantle and crustal magmas as revealed by single crystal analysis. Reviews in Mineralogy and Geochemistry, 69, 445–478.

Bonamici C.E., Kozdon R., Ushikubo T. and Valley J.W. (2011)
High-resolution *P-T-t* paths from $\delta^{18}O$ zoning in titanite: A snapshot of late-orogenic collapse in the Grenville of New York. Geology, 39, 959–962.

Boudier F., Baronnet A. and Mainprice D. (2010)
Serpentine mineral replacements of natural olivine and their seismic implications: Oceanic lizardite versus subduction-related antigorite. Journal of Petrology, 51, 495–512.

Coggon J., Matter J., Kelemen P., Teagle D. and the Oman Drilling Project Science Party (2020) Overview of the Oman Drilling Project. International Conference on Ophiolites and the Oceanic Lithosphere: Results of the Oman Drilling Project and Related Research (Muscat, Sultanate of Oman), 12–14 January 2020.

Debret B., Bolfan-Casanova N., Padrón-Navarta J.A., Martin-Hernandez F., Andreani M., Garrido C.J., López S.-V., Gómez-Pugnaire M.T., Muñoz M. and Trcera N. (2015)
Redox state of iron during high-pressure serpentinite dehydration. Contributions to Mineralogy and Petrology, 169, 1–18.

Deloule E., France-Lanord C. and Albarède F. (1991)
D/H analysis of minerals by ion probe. In: Taylor Jr. H.P., O'Neil J.R. and Kaplan I.R. (eds), Stable isotope geochemistry: A tribute to Samuel Epstein. The Geochemical Society, Special Publication, 3, 53–62.

Deschamps F., Guillot S., Godard M., Chauvel C., Andreani M. and Hattori K. (2010)
In situ characterization of serpentinites from forearc mantle wedges: Timing of serpentinization and behavior of fluid-mobile elements in subduction zones. Chemical Geology, 269, 262–277.

Dewandel B., Boudier F., Kern H., Warsi W. and Mainprice D. (2003)
Seismic wave velocity and anisotropy of serpentinized peridotite in the Oman ophiolite. Tectonophysics, 370, 77–94.

Dietrich V. (1972)
Ilvait, Ferroantigorit und Greenalith als Begleiter oxidisch-sulfidischer Vererzungen in den Oberhalbsteiner Serpentiniten. Schweizerische Mineralogische Und Petrogrographische Mitteilungen, 52, 57–78.

Donovan J.J., Kremser D., Fournelle J. and Goemann K. (2019)
Probe for EPMA – User's guide and reference manual. Probe Software Inc. (Eugene), 429pp.

Donovan J.J. and Tingle T.N. (1996)
An improved mean atomic number background correction for quantitative microanalysis. Microscopy and Microanalysis, 2, 1–7.

Evans B.W., Dyar M.D. and Kuehner S.M. (2012)
Implications of ferrous and ferric iron in antigorite. American Mineralogist, 97, 184–196.

Evans B.W., Hattori K. and Baronnet A. (2013)
Serpentinite: What, why, where? Elements, 9, 99–106.

Evans B.W., Kuehner S.M. and Chopelas A. (2009)
Magnetite-free, yellow lizardite serpentinization of olivine websterite, Canyon Mountain complex, N.E. Oregon. American Mineralogist, 94, 1731–1734.

Falk E.S., Guo W., Paukert A.N., Matter J.M., Mervine E.M. and Kelemen P.B. (2016)
Controls on the stable isotope compositions of travertine from hyperalkaline springs in Oman: Insights from clumped isotope measurements. Geochimica et Cosmochimica Acta, 192, 1–28.

Falk E.S. and Kelemen P.B. (2015)
Geochemistry and petrology of listvenite in the Samail ophiolite, Sultanate of Oman: Complete carbonation of peridotite during ophiolite emplacement. Geochimica et Cosmochimica Acta, 160, 70–90.

Faust G.T. and Fahey J.J. (1962)
The serpentine-group minerals. U.S. Geological Survey Professional Paper, 384A, 1–92.

references

Fleitmann D., Burns S.J., Pekala M., Mangini A., Al-Subbary A., Al-Aowah M., Kramers J. and Matter A. (2011)
Holocene and Pleistocene pluvial periods in Yemen, southern Arabia. Quaternary Science Reviews, 30, 783–787.

Früh-Green G.L., Connolly J.A.D., Plas A., Kelley D.S. and Grobéty B. (2004)
Serpentinization of oceanic peridotites: Implication for geochemical cycles and biological activity. Geophysical Monograph Series, 144, 119–136.

Früh-Green G.L., Grabowska M., Oyanagi R., Kimura K., Morishita T., Okamoto A., Klein F., Tamura A., Teagle D.A.H., Takazawa E., Coggon J.A., Kelemen P.B., and Matter J.M. (2018)
Hydrothermal alteration of the crust-mantle transition and upper mantle in the Samail ophiolite: Insights from Holes CM1A and CM2B of the Oman Drilling Project. American Geophysical Union, Fall Meeting 2018, abstract #V11B-02.

Früh-Green G.L., Plas A. and Lecuyer C. (1996)
Petrologic and stable isotope constraints on hydrothermal alteration and serpentinization of the EPR shallow mantle at Hess Deep (Site 895). In: Mével C., Gillis K.M., Allan J.F. and Meyer P.S. (eds), Proceedings of the Ocean Drilling Program: Scientific Results, 147, 255–291.

Gauthiez-Putallaz L., Rubatto D. and Hermann J. (2016)
Dating prograde fluid pulses during subduction by *in situ* U-Pb and oxygen isotope analysis. Contributions to Mineralogy and Petrology, 171, 1–20.

Godard M., Dautria J.M. and Perrin M. (2003)
Geochemical variability of the Oman ophiolite lavas: Relationship with spatial distribution and paleomagnetic directions. Geochemistry Geophysics Geosystems, 4, 1–15.

Gregory R.T. and Taylor H.P. (1981)
An oxygen isotope profile in a section of Cretaceous oceanic crust, Samail Ophiolite, Oman: Evidence for $\delta^{18}O$ buffering of the oceans by deep (>5 km) seawater-hydrothermal circulation at mid-ocean ridges. Journal of Geophysical Research, 86, 2737–2755.

Hacker B.R., Mosenfelder J.L. and Gnos E. (1996)
Rapid emplacement of the Oman ophiolite: Thermal and geochronologic constraints. Tectonics, 15, 1230–1247.

Hattori K.H. and Guillot S. (2007)
Geochemical character of serpentinites associated with high- to ultrahigh-pressure metamorphic rocks in the Alps, Cuba, and the Himalayas: Recycling of elements in subduction zones. Geochemistry, Geophysics Geosystems, 8, 1–27.

Hess H.H., Smith R.J. and Dengo G. (1952)
Antigorite from the vicinity of Caracas, Venezuela. American Mineralogist, 37, 68–75.

Hoefs J. (2018)
Stable isotope geochemistry (8th edition). Springer (Berlin), 437pp.

Huberty J.M., Kita N.T., Kozdon R., Heck P.R., Fournelle J.H., Spicuzza M.J., Xu H. and Valley J.W. (2010)
Crystal orientation effects in $\delta^{18}O$ for magnetite and hematite by SIMS. Chemical Geology, 276, 269–283.

Isa J., Kohl I.E., Liu M.C., Wasson J.T., Young E.D. and McKeegan K.D. (2017)
Quantification of oxygen isotope SIMS matrix effects in olivine samples: Correlation with sputter rate. Chemical Geology, 458, 14–21.

Jones D., Hartley J., Frisch G., Purnell M. and Darras L. (2012)
Non-destructive, safe removal of conductive metal coatings from fossils: A new solution. Paleontologia Electronica, 15, 1–7.

Kahl W.A., Jöns N., Bach W., Klein F. and Alt J.C. (2015)
Ultramafic clasts from the South Chamorro serpentine mud volcano reveal a polyphase serpentinization history of the Mariana forearc mantle. Lithos, 227, 1–20.

Kelemen P.B., Bach W., Beinlinch A., Cai M., Choe S., Coggon J., de Obeso J.C., Ellison E., Eslami A., Evans K., Godard M., Harris M., Hirth G., Kahl W.A., Malvoisin B., Manning C., Matter J., Michibayashi K., Okazaki K., Pezard P., Teagle D., Templeton A., Urai J. and Zhu W. and the Oman Drilling project Science Team (2020a)
Alteration of peridotite in the Samail ophiolite: Results from the Oman Drilling Project. International Conference on Ophiolites and the Oceanic Lithosphere: Results of the Oman Drilling Project and Related Research (Muscat, Sultanate of Oman), 12–14 January 2020.

Kelemen P.B., Bach W., Evans K.A., Eslami A., Farough A., Hamada M., Ychiyama Y., Kahl W.A., Matter J.M., Pezard P.A., Paukert Vankeuren A.N., Godard M., Michibayashi K., Choe S. and Coggon J.A. (2018)
Correlated variation in vein type, vein frequency, pH, oxygen fugacity and depth in Oman Drilling Project Holes BA1B, BA3A and BA4A. American Geophysical Union, Fall Meeting 2018, abstract #V12B-03.

Kelemen P.B., Choe S., Coggon J., Godard M., Michibayashi K., Matter J., Teagle D., Templeton A. and the Oman Drilling project Science Team (2020b)
Geology of the Multi-Borehole Observatory: Holes BA1A, B, C, BA2A, BA3A and BA4A in altered mantle peridotite. International Conference on Ophiolites and the Oceanic Lithosphere: Results of the Oman Drilling Project and Related Research (Muscat, Sultanate of Oman), 12–14 January 2020.

Kelemen P.B. and Matter J. (2008)
In situ carbonation of peridotite for CO_2 storage. Proceedings of the National Academy of Sciences, 105, 17295–17300.

Kelemen P.B., Matter J., Streit E.E., Rudge J.F., Curry W.B. and Blusztajn J. (2011)
Rates and mechanisms of mineral carbonation in peridotite: Natural processes and recipes for enhanced, *in situ* CO_2 capture and storage. Annual Review of Earth and Planetary Science, 39, 545–576.

references

Kelley D.S., Karson J.A., Früh-Green G.L., Yoerger D.R., Shank T.M., Butterfield D.A., Hayes J.M., Schrenk M.O., Olson E.J., Proskurowski G., Jakuba M., Bradley A., Larson B., Ludwig K., Glickson D., Buckman K., Bradley A.S., Brazelton W.J., Roe K., Elend M.J., Delacour A., Bernasconi S.M., Lilley M.D., Baross J.A., Summons R.E. and Sylva S.P. (2005)
A serpentinite-hosted ecosystem: The Lost City hydrothermal field. Science, 307, 1428–1434.

Kelly J.L., Fu B., Kita N.T. and Valley J.W. (2007)
Optically continuous silcrete quartz cements of the St. Peter Sandstone: High precision oxygen isotope analysis by ion microprobe. Geochimica et Cosmochimica Acta, 71, 3812–3832.

Kita N.T., Huberty J.M., Kozdon R., Beard B.L. and Valley J.W. (2011)
High-precision SIMS oxygen, sulfur and iron stable isotope analyses of geological materials: Accuracy, surface topography and crystal orientation. Surface and Interface Analysis, 43, 427–431.

Kita N.T., Nagahara H., Tachibana S., Tomomura S., Spicuzza M.J., Fournelle J.H. and Valley J.W. (2010)
High precision SIMS oxygen three isotope study of chondrules in LL3 chondrites: Role of ambient gas during chondrule formation. Geochimica et Cosmochimica Acta, 74, 6610–6635.

Kita N.T., Ushikubo T., Fu B. and Valley J.W. (2009)
High precision SIMS oxygen isotope analysis and the effect of sample topography. Chemical Geology, 264, 43–57.

Kozdon R., Kita N.T., Huberty J.M., Fournelle J.H., Johnson C.A. and Valley J.W. (2010)
In situ sulfur isotope analysis of sulfide minerals by SIMS: Precision and accuracy, with application to thermometry of ~ 3.5 Ga Pilbara chert. Chemical Geology, 275, 243–253.

Kozdon R., Ushikubo T., Kita N.T., Spicuzza M. and Valley J.W. (2009)
Intratest oxygen isotope variability in the planktonic foraminifer *N. pachyderma*: Real vs. apparent vital effects by ion microprobe. Chemical Geology, 258, 327–337.

Marchesi C., Garrido C.J., Padrón-Navarta J.A., López S.-V. and Gómez-Pugnaire M.T. (2013)
Element mobility from seafloor serpentinization to high-pressure dehydration of antigorite in subducted serpentinite: Insights from the Cerro del Almirez ultramafic massif (southern Spain). Lithos, 178, 128–142.

Martin L.A.J., Rubatto D., Crépisson C., Hermann J., Putlitz B. and Vitale-Brovarone A. (2014)
Garnet oxygen analysis by SHRIMP-SI: Matrix corrections and application to high-pressure metasomatic rocks from Alpine Corsica. Chemical Geology, 374–375, 25–36.

Mayhew L.E. and Ellison E.T. (2020)
A synthesis and meta-analysis of the Fe chemistry of serpentinites and serpentine minerals. Philosophical Transactions of the Royal Society, A378, 1–29.

McCollom T.M. and Seewald J.S. (2013)
Serpentinites, hydrogen, and life. Elements, 9, 129–134.

Miller H.M., Matter J.M., Kelemen P., Ellison E.T., Conrad M.E., Fierer N., Ruchala T., Tominaga M. and Templeton A.S. (2016)
Modern water/rock reactions in Oman hyperalkaline peridotite aquifers and implications for microbial habitability. Geochimica et Cosmochimica Acta, 179, 217–241.

Nasir S., Al Sayigh R.A., Al H.A., Al-Khirbash S., Al-Jaaidi O., Musllam A., Al-Mishwat A. and Al-Bu'saidi S. (2007)
Mineralogical and geochemical characterization of listwaenite from the Semail Ophiolite, Oman. Chemie Der Erde, 67, 213–228.

Neal C. and Stanger G. (1984)
Calcium and magnesium hydroxide precipitation from alkaline groundwaters in Oman, and their significance to the process of serpentinization. Mineralogical Magazine, 48, 237–241.

Neal C. and Stanger G. (1985)
Past and present serpentinisation of ultramafic rocks: An example from the Semail ophiolite nappe of northern Oman. The Chemistry of Weathering, 149, 249–275.

Nicholson S.L., Pike A.W.G., Hosfield R., Roberts N., Sahy D., Woodhead J., Cheng H., Edwards R.L., Affolter S., Leuenberger M., Burns S.J., Matter A. and Fleitmann D. (2020)
Pluvial periods in southern Arabia over the last 1.1 million-years. Quaternary Science Reviews, 229, 1–17.

Noël J., Godard M., Oliot E., Martinez I., Williams M., Boudier F., Rodriguez O., Chaduteau C., Escario S. and Gouze P. (2018)
Evidence of polygenetic carbon trapping in the Oman ophiolite: Petro-structural, geochemical, and carbon and oxygen isotope study of the Wadi Dima harzburgite-hosted carbonates (Wadi Tayin Massif, Sultanate of Oman). Lithos, 323, 218–237.

O'Hanley D.S. (1996)
Serpentinites: Records of tectonic and petrological history. Oxford Monographs on Geology and Geophysics, 24. Oxford University Press (New York), 277pp.

Page F.Z., Kita N.T. and Valley J.W. (2010)
Ion microprobe analysis of oxygen isotopes in garnets of complex chemistry. Chemical Geology, 270, 9–19.

Paukert Vankeuren A.N., Matter J.M., Stute M. and Kelemen P.B. (2019)
Multitracer determination of apparent groundwater ages in peridotite aquifers within the Samail ophiolite, Sultanate of Oman. Earth and Planetary Science Letters, 516, 37–48.

Petriglieri J.R., Salvioli-Mariani E., Mantovani L., Tribaudino M., Lottici P.P., Laporte-Magoni C. and Bersani D. (2015)
Micro-Raman mapping of the polymorphs of serpentine. Journal of Raman Spectroscopy, 46, 953–958.

Pollington A.D. (2013)
Stable isotope signatures of diagenesis: Natural and experimental studies. Ph.D. thesis, University of Wisconsin, Madison.

references

Putlitz B., Katzir Y., Matthews A. and Valley J.W. (2001)
Oceanic and orogenic fluid-rock interaction in $^{18}O/^{16}O$-enriched metagabbros of an ophiolite (Tinos, Cyclades). Earth and Planetary Science Letters, 193, 99–113.

Ramsay J.G. (1980)
The crack-seal mechanism of rock deformation. Nature, 284, 135–139.

Reynard B. and Wunder B. (2006)
High-pressure behavior of synthetic antigorite in the MgO-SiO_2-H_2O system from Raman spectroscopy. American Mineralogist, 91, 459–462.

Rinaudo C., Gastaldi D. and Belluso E. (2003)
Characterization of chrysotile, antigorite and lizardite by FT-Raman spectroscopy. The Canadian Mineralogist, 41, 883–890.

Rioux M., Bowring S., Kelemen P., Gordon S., Dudás F. and Miller R. (2012)
Rapid crustal accretion and magma assimilation in the Oman-U.A.E. ophiolite: High precision U-Pb zircon geochronology of the gabbroic crust. Journal of Geophysical Research, 117, 1–12.

Rioux M., Bowring S., Kelemen P., Gordon S., Miller R. and Dudás F. (2013)
Tectonic development of the Samail ophiolite: High-precision U-Pb zircon geochronology and Sm-Nd isotopic constraints on crustal growth and emplacement. Journal of Geophysical Research, 118, 2085–2101.

Rollion-Bard C. and Marin-Carbonne J. (2011)
Determination of SIMS matrix effects on oxygen isotopic compositions in carbonates. Journal of Analytical Atomic Spectrometry, 26, 1285–1289.

Rouméjon S., Williams M.J. and Früh-Green G.L. (2018)
In-situ oxygen isotope analyses in serpentine minerals: Constraints on serpentinization during tectonic exhumation at slow- and ultraslow-spreading ridges. Lithos, 323, 156–173.

Rubatto D., Putlitz B., Gauthiez-Putallaz L., Crépisson C., Buick I.S. and Zheng Y.F. (2014)
Measurement of in-situ oxygen isotope ratios in monazite by SHRIMP ion microprobe: Standards, protocols and implications. Chemical Geology, 380, 84–96.

Saccocia P.J., Seewald J.S. and Shanks W.C. (2009)
Oxygen and hydrogen isotope fractionation in serpentine-water and talc-water systems from 250 to 450 °C, 50 MPa. Geochimica et Cosmochimica Acta, 73, 6789–6804.

Savin S.M. and Lee M. (1988)
Isotopic studies of phyllosilicates. In: Bailey S.W. (ed.), Hydrous phyllosilicates. Reviews in Mineralogy, 19, 189–223.

Scambelluri M., Fiebig J., Malaspina N., Müntener O. and Pettke T. (2004)
Serpentinite subduction: Implications for fluid processes and trace-element recycling. International Geology Review, 46, 595–613.

Schmitt A.K., Chamberlain K.R., Swapp S.M. and Harrison T.M. (2010)
In situ U-Pb dating of micro-baddeleyite by secondary ion mass spectrometry. Chemical Geology, 269, 386–395.

Schrenk M.O., Brazelton W.J. and Lang S.Q. (2013)
Serpentinization, carbon, and deep life. Reviews in Mineralogy and Geochemistry, 75, 575–606.

Schulze D.J., Harte B., Valley J.W., Brenan J.M., De R. and Channer D.M. (2003)
Extreme crustal oxygen isotope signatures preserved in coesite in diamond. Nature, 423, 68–70.

Schwarzenbach E.M., Früh-Green G.L., Bernasconi S.M., Alt J.C. and Plas A. (2013)
Serpentinization and carbon sequestration: A study of two ancient peridotite-hosted hydrothermal systems. Chemical Geology, 351, 115–133.

Scicchitano M.R., Rubatto D., Hermann J., Majumdar A.S. and Putnis A. (2018b)
Oxygen isotope analysis of olivine by ion microprobe: Matrix effects and applications to a serpentinised dunite. Chemical Geology, 499, 126–137.

Scicchitano M.R., Rubatto D., Hermann J., Shen T., Padrón-Navarta J.A., Williams I.S. and Zheng Y.-F. (2018a)
In situ oxygen isotope determination in serpentine minerals by ion microprobe: Reference materials and applications to ultrahigh-pressure serpentinites. Geostandards and Geoanalytical Research, 42, 459–479.

Senda R., Carter E., Zaloumis J., Zhang C., Sousa A., Klaessens D., Godard M., Kelemen P., Michibayashi K., Teagle D., Takazawa E., Coggon J., Choe S. and the Oman Drilling Project Phase 2 Science Party (2020)
Geochemistry of the Samail ophiolite mantle section drilled at Oman Drilling Project phase 2, Holes BA1B, BA3A and BA4A ~ preliminary results on board. International Conference on Ophiolites and the Oceanic Lithosphere: Results of the Oman Drilling Project and Related Research. Muscat, Sultanate of Oman, 12–14 January 2020.

Siron G., Baumgartner L., Bouvier A.-S., Putlitz B. and Vennemann T. (2017)
Biotite reference materials for secondary ion mass spectrometry $^{18}O/^{16}O$ measurements. Geostandards and Geoanalytical Research, 41, 243–253.

Sleep N.H., Meibom A., Fridriksson T.H., Coleman R.G. and Bird D.K. (2004)
H_2-rich fluids from serpentinization: Geochemical and biotic implications. Proceedings of the National Academy of Sciences, 101, 12818–12823.

Śliwiński M.G., Kitajima K., Kozdon R., Spicuzza M.J., Fournelle J.H., Denny A. and Valley J.W. (2015)
Secondary ion mass spectrometry bias on isotope ratios in dolomite–ankerite, Part I: $\delta^{18}O$ matrix effects. Geostandards and Geoanalytical Research, 40, 157–172.

references

Śliwiński M.G., Kitajima K., Spicuzza M.J., Orland I.J., Ishida A., Fournelle J.H. and Valley J.W. (2017)
SIMS bias on isotope ratios in Ca-Mg-Fe carbonates (Part III): $\delta^{18}O$ and $\delta^{13}C$ matrix effects along the magnesite–-siderite solid-solution series. Geostandards and Geoanalytical Research, 42, 49–76.

Spicuzza M.J., Valley J.W. and McConnell V.S. (1998)
Oxygen isotope analysis of whole rock via laser fluorination: An air-lock approach. Geological Society of America Abstract Progress, 30, 80.

Stanger G. (1985)
Silicified serpentinite in the Semail nappe of Oman. Lithos, 18, 13–22.

Streit E., Kelemen P. and Eiler J. (2012)
Coexisting serpentine and quartz from carbonate-bearing serpentinized peridotite in the Samail Ophiolite, Oman. Contributions to Mineralogy and Petrology, 164, 821–837.

Tarling M.S., Rooney J.S., Viti C., Smith S.A.F. and Gordon K.C. (2018)
Distinguishing the Raman spectrum of polygonal serpentine. Journal of Raman Spectroscopy, 49, 1978–1984.

Taylor R., Clark C. and Reddy S.M. (2012)
The effect of grain orientation on secondary ion mass spectrometry (SIMS) analysis of rutile. Chemical Geology, 300–301, 81–87.

Teagle D.A.H., Kelemen P.B., Matter J.M., Templeton A.S. and Coggon J.A. (2018)
Introduction to the Oman Drilling Project. American Geophysical Union, Fall Meeting 2018, abstract #V13E-0151.

Tenner T.J., Kimura M. and Kita N.T. (2017)
Oxygen isotope characteristics of chondrules from the Yamato-82094 ungrouped carbonaceous chondrite: Further evidence for common O-isotope environments sampled among carbonaceous chondrites. Meteoritics and Planetary Science, 52, 268–294.

Tenner T.J., Nakashima D., Ushikubo T., Kita N.T. and Weisberg M.K. (2015)
Oxygen isotope ratios of FeO-poor chondrules in CR3 chondrites: Influence of dust enrichment and H_2O during chondrule formation. Geochimica et Cosmochimica Acta, 148, 228–250.

Uehara S. (1998)
TEM and XRD study of antigorite superstructures. The Canadian Mineralogist, 36, 1595–1605.

Uehara S. and Kamata K. (1994)
Antigorite with a large supercell from Saganoseki, Oita Prefecture, Japan. The Canadian Mineralogist, 32, 93–103.

Uehara S. and Shirozu H. (1985)
Variations in chemical composition and structural properties of antigorites. Mineralogical Journal, 12, 299–318.

Valley J.W. and Kita N.T. (2009)
In situ oxygen isotope geochemistry by ion microprobe. Mineralogical Association of Canada Shortcourse Series, 41, 19–63.

Valley J.W., Kitchen N., Kohn M.J., Niendorf C.R. and Spicuzza M.J. (1995)
UWG-2, a garnet standard for oxygen isotope ratios: Strategies for high precision and accuracy with laser heating. Geochimica et Cosmochimica Acta, 59, 5223–5231.

Valley J.W., Lackey J.S., Cavosie A.J., Clechenko C.C., Spicuzza M.J., Basei M.A.S., Bindeman I.N., Ferreira V.P., Sial A.N., King E.M., Peck W.H., Sinha A.K. and Wei C.S. (2005)
4.4 billion years of crustal maturation: Oxygen isotope ratios of magmatic zircon. Contributions to Mineralogy and Petrology, 150, 561–580.

Vielzeuf D., Champenois M., Valley J.W., Brunet F. and Devidal J.L. (2005)
SIMS analysis of oxygen isotopes: matrix effects in Fe-Mg-Ca garnets. Chemical Geology, 223, 208–226.

Wenner D.B. and Taylor H.P. (1971)
Temperatures of serpentinization of ultramafic rocks based on O^{18}/O^{16} fractionation between coexisting serpentine and magnetite. Contributions to Mineralogy and Petrology, 32, 165–185.

Wenner D.B. and Taylor H.P. (1973)
Oxygen and hydrogen isotope studies of the serpentinization of ultramafic rocks in oceanic environments and continental ophiolite complexes. American Journal of Science, 273, 207–239.

Wenner D.B. and Taylor H.P. (1974)
D/H and O^{18}/O^{16} studies of serpentinization of ultramafic rocks. Geochimica et Cosmochimica Acta, 38, 1255–1286.

Wingate M.T.D. and Compston W. (2000)
Crystal orientation effects during ion microprobe U-Pb analysis of baddeleyite. Chemical Geology, 168, 75–97.

Zhang X., Yang S., Zhao H., Jiang S., Zhang R. and Xie J. (2019)
Effect of beam current and diameter on electron probe microanalysis of carbonate minerals. Journal of Earth Science, 30, 834–842.

Zheng Y.-F. (1993)
Calculation of oxygen isotope fractionation in hydroxyl-bearing silicates. Earth and Planetary Science Letters, 120, 247–263.

Supporting information

The following supporting information may be found in the online version of this article:

Figure S1. Reflected light images of new antigorite reference materials (UWSrp-1 to 9) along with lizardite L3431, chrysotile C22908, calcite UWC-3, garnet UWG-2, quartz UWQ-1, and zircon KIM-5 and UWZ-1.

Figure S2. Raman (a) SiO- and (b) OH-stretching bands for the new antigorite reference materials.

Figure S3. *X-Y* coordinates of pits in chrysotile with the elongation of fibres parallel or perpendicular to the surface of the mount during two measurement sessions.

Figure S4a. Representative Raman maps in four different areas of sample BA1B-400

Figure S4b. Representative Raman maps in one area of sample BA1B-20

Figure S5. Diagrams showing the chemical composition of different serpentine generations in samples BA1B-400 and BA1B-20 in terms of (a, d) Mg#, (b, e) Al_2O_3, and (c, f) MgO + FeO *versus* SiO_2.

Figure S6. Diagram showing no correlation between oxygen isotope composition and MgO + FeO(total) for all serpentine generations in sample BA1B-400.

Table S1. Summary of SIMS data (bias, 2s, 2SE, bias* relative to antigorite Al06-44A) for new serpentine reference materials determined by CAMECA 1280.

Table S2. Complete data table of oxygen isotope analyses acquired by CAMECA 1280 in the serpentine reference materials along with calculations of the matrix bias calibration due to Mg/Fe variation in antigorite [bias*(*x*)] and grain orientation effects in antigorite and chrysotile.

Table S3. Complete data table of oxygen isotope (S3a) and EPMA data (S3b) acquired in serpentine from samples BA1B-20 and BA1B-400, Samail Ophiolite.

This material is available from: http://onlinelibrary.wiley.com/doi/10.1111/ggr.12359/abstract (This link will take you to the article abstract).